

1 **A global view of the stratospheric background, volcanic and** 2 **wildfire aerosol in the CALIOP era (2006 – 2023)**

3 Bengt G. Martinsson, Johan Friberg, and Moa K. Sporre

4 Department of Physics, Lund University, Lund, Sweden

5 *Correspondence to:* Bengt G. Martinsson (bengt.martinsson@fysik.lu.se)

6 **Abstract.** This study deals with the stratospheric aerosol during the 17 years of lidar
7 measurements with CALIOP aboard the CALIPSO satellite. To obtain extinction from the
8 backscattering measurements, we estimated the lidar ratios of the main aerosol
9 injections into the stratosphere. The stratospheric background is estimated by making a
10 subdivision of the stratosphere into nine parts, spanned by three latitude and altitude
11 intervals, reaching background conditions individually at different times. The extracted
12 background estimate shows excellent agreement with SAGE II solar occultation
13 measurements in the volcanically quiescent period 1998 - 2000. Our results show that
14 70% of the background aerosol in the deep Brewer-Dobson (dBD) branch is formed
15 above 19 km altitude, indicating strong influence of carbonyl sulfide on the
16 stratospheric background aerosol. The stratosphere was clearly affected by 15 volcanic
17 eruptions and 5 wildfires. Their combined aerosol load affected the Southern
18 extratropics, tropics and Northern extratropics almost equally, and the altitude
19 distribution shows that the shallow Brewer-Dobson branch was most affected (43%)
20 followed by the dBD (31%) and lowermost stratosphere (26%). The most important
21 events in order of maximum AOD were the Hunga Ha’apai eruption (2022), Australian
22 wildfires (2019-20) and the eruptions of Raikoke (2019), Sarychev (2009) and Nabro
23 (2011). These events induced strong variability in the yearly average global stratospheric
24 aerosol optical depth (AOD), which ranged from 0.0057 (background) to 0.016. CALIOP
25 provided invaluable data for stratospheric aerosol climatologies during its 17 years of
26 operation.

27 **1. Introduction**

28 Tropospheric air, containing aerosol particles and the sulfurous aerosol precursor gases
29 carbonyl sulfide (OCS) and sulfur dioxide (SO₂), enter the stratosphere across the

30 tropical tropopause. These constituents form the stratospheric background aerosol
31 (Kremser et al., 2016), an aerosol layer that is located above 20 km altitude in the
32 tropics, and lower in the extratropics, containing water-soluble sulfur-rich particles
33 (Junge et al., 1961). Additional aerosol, that can be classified as background due to its
34 diffuse nature, originates from the Asian Tropopause Aerosol Layer (ATAL), an aerosol
35 layer between 13 – 18 km altitude over Asia (Vernier et al., 2015). The stratospheric
36 background aerosol contains sulfate, water, organics, and minor traces of tropospheric
37 aerosol and extraterrestrial material (Martinsson et al., 2005; Murphy et al., 2007;
38 Kremser et al., 2016; Martinsson et al., 2019).

39 The stratospheric aerosol load is highly variable due to special aerosol events
40 connected to volcanism (Bauman et al., 2003; Vernier et al., 2009; Solomon et al., 2011;
41 Andersson et al., 2015) and wildfires (Fromm et al., 2010; Baars et al., 2019; Ohneiser et
42 al., 2020; Peterson et al., 2021; Martinsson et al., 2022; Solomon et al., 2022; Friberg et
43 al., 2023, Peterson et al., 2025), which inject copious amounts of aerosol and precursor
44 gases affecting the stratospheric aerosol for months up to several years (Friberg et al.,
45 2018). These aerosol events induce a variability that needs to be accounted for in
46 climate models. From 1979, the satellite measurement era, the most important
47 volcanic eruptions, El Chichon in 1982 and Mt. Pinatubo (1991), caused a maximum
48 global 3-month average effective radiative forcing of -2 and -3 W/m², respectively
49 (Schmidt et al., 2018). After a period of low volcanic influence on the stratosphere
50 around the turn of the millennium, many volcanic eruptions and wildfires have affected
51 the aerosol in the stratosphere. The most important are the 2019-20 Australian wildfires
52 and the eruptions of Sarychev (2009), Raikoke (2019) and Hunga Ha’apai (2022).

53 Fresh wildfire aerosol particles contain black carbon and a dominating fraction of
54 organics (Garofalo et al., 2019), where the latter is rapidly lost (half-life 10 days) in the
55 stratosphere due to photolysis (Martinsson et al., 2022). The composition of volcanic
56 stratospheric aerosol particles varies. SO₂-rich volcanic emissions, like the 2008
57 eruption of Kasatochi, are dominated by sulfate, some organics and a minor fraction of
58 ash (Martinsson et al., 2009, Andersson et al., 2013; Friberg et al., 2014). On the other
59 hand, SO₂-poor eruptions, like that of Puyehue-Cordón Caulle in 2011, are dominated
60 by ash (Clarisse et al., 2013). Steam-boosted eruptions of submarine volcanoes (Mastin

61 et al., 2024), like the 2022 eruption of Hunga Ha’apai, can result in a stratospheric
62 aerosol with a strong contribution from sea salt (Martinsson et al., 2025).

63 From the beginning of extensive satellite data in the late 1970s the stratospheric aerosol
64 load has usually been measured using solar occultation (Sato et al., 1993). GloSSAC
65 (Global Space-based Stratospheric Aerosol Climatology), a later construction of a
66 continuous record of optical properties of stratospheric aerosol spanning 1979 to
67 present, has a core of solar occultation measurement with the notable 22 year era of
68 SAGE II continuing a few years of solar occultation measurement by SAM II and SAGE I
69 (Thomason et al., 2018). Solar occultation became unavailable during 2005 – 2017. To
70 continue the GloSSAC record, other satellite-based measurements were deployed. The
71 limb scatter instrument OSIRIS (Rieger et al., 2015) and the lidar CALIOP (Cloud-Aerosol
72 Lidar with Orthogonal Polarization) (Winker et al., 2010) were, after substantial
73 recalibration (Thomason et al., 2018, Kovilakam et al., 2020, Kovilakam et al., 2023),
74 used to bridge the gap to obtain continuous time series of stratospheric aerosol
75 properties. Mixing data from many sources that are relying on different measurement
76 principles is however complex, as pointed out by Thomason et al. (2018). We will return
77 to this matter in the discussion section.

78 This work deals with the stratospheric aerosol in the CALIOP era, spanning the 17-year
79 period 2006-06-12 to 2023-06-30. CALIOP data (level 1B, version 4-51) is corrected for
80 attenuation, and the lidar ratio is estimated for the stratospheric aerosol resulting from
81 12 volcanic eruptions and wildfires. The stratosphere from the tropopause to 35 km
82 altitude is divided into three altitude and three latitude parts, in total nine parts, where
83 the backscattering of the background stratospheric aerosol is identified and its sources
84 discussed. By subtraction of the signal from the background aerosol, the backscattering
85 from major stratospheric aerosol events is obtained. This is converted to AOD using the
86 estimated lidar ratios. We find that global average aerosol backscattering intensity
87 exceeded the background by 55% in the 17 years studied. The strongest influence from
88 volcanism and wildfires was in 2022 and 2023 due to the submarine Hunga Ha’apai
89 eruption. The second strongest occurred in 2020 due to the Australian wildfires,
90 followed by 2009 (Sarychev eruption) and 2019 (mainly the Raikoke eruption). 2013 was
91 a year when the entire stratosphere was close to background conditions. Finally, we

92 discuss the validity of lidar data in comparison with the more established data based on
93 solar occultation.

94 **2. Methods**

95 This paper is based on measurements with the CALIOP lidar instrument aboard the
96 CALIPSO (Cloud-Aerosol Lidar and Infrared Pathfinder Satellite Observation) satellite
97 that completed approximately 15 orbits between latitudes -82 and 82° each day.

98 ***2.1 CALIOP properties and methods applied***

99 CALIOP with a laser of 532 nm wavelength produced vertical profiles of backscattering
100 intensity from air molecules, aerosol particles and cloud drops from the ground up to 35
101 km altitude with high vertical resolution depending on altitude. In the altitude ranges <
102 8.2, 8.2 - 20.2, 20.2 – 30.1 and >30.1 km the vertical resolution is 30, 60, 180 and 300 m,
103 respectively (Winker et al., 2007, 2010). Here we use data only from the stratosphere,
104 where the tropopause altitude according to MERRA-2 reanalysis (Modern-Era
105 Retrospective analysis for Research and Applications) (Gelaro et al., 2017) was used to
106 discriminate data from the troposphere. Only data recorded during nighttime were used
107 in the general evaluation concerning all the CALIOP data available (Friberg et al., 2018;
108 Martinsson et al., 2022), implying that data will be missing at high latitudes for part of
109 the year with the strongest influence at the summer solstice. Data are also missing at
110 high latitudes mainly in the southern hemisphere due to influence from polar
111 stratospheric clouds. The data were extrapolated linearly to cover all the way to 80°
112 latitude in both hemispheres. In the global perspective used here the fraction of the
113 earth's surface area affected by the extrapolation is 8.7% at the summer solstice and
114 3.5% two months before/after that time. In most cases the quantitative impact on the
115 global AOD is small, but in special cases, like the eruption of the Icelandic volcano
116 Grimsvötn (64° N) on 21 May 2011, the inability to measure at high latitudes causes
117 larger quantitative errors (Andersson et al., 2015).

118 The evaluation is based on version 4-51 of CALIOP level 1B data (NASA/LARC/SD/ASDC,
119 2024). Clouds within 3km above the tropopause were discriminated based on
120 depolarization of the signal obtained from the CALIOP instrument, polar stratospheric

121 clouds were discriminated based on temperature and data taken in the South Atlantic
122 Anomaly are filtered out as explained in Friberg et al. (2018) and Martinsson et al.
123 (2022). The backscatter data were corrected for attenuation by methodology described
124 in Martinsson et al. (2022) and were first converted to extinction by the standard
125 effective lidar ratio $S = 50$ sr used for CALIOP (Kar et al., 2019). Volcanic eruptions and
126 wildfires with lidar ratio deviating from 50 sr by more than 5% were corrected, see
127 sections 2.3 and 3.4.

128 The stratospheric CALIOP level 3 product (Kar et al., 2019) and the data presented here
129 are both based on the CALIOP level 1B data set but differ with respect to latitude-,
130 longitude- and time-resolution, where CALIOP level 3 is based on monthly averages and
131 we normally use a time-resolution of 1 – 8 days depending on issue investigated. These
132 data sets also differ with respect to lidar ratios: CALIOP level 3 extinction is obtained
133 based on a fixed lidar ratio of 50 sr, whereas we, when possible, estimate effective lidar
134 ratios for aerosol from individual volcanic eruptions and wildfires as described in
135 sections 2.3, 3.1 and 3.4. The notion “effective” relates to that CALIOP is affected by
136 multiple scattering, implying that use of lidar ratios for measurements unaffected by
137 multiple scattering, i.e., the true physical relation between extinction and
138 backscattering of the aerosol studied, will result in overestimation the extinction (Prata
139 et al., 2017; Martinsson et al., 2022). Another difference between CALIOP level 3 and
140 our method is that we correct data for attenuation of the detected scattered light
141 (Martinsson et al., 2022), which is important for identification and quantification of
142 aerosol processes in wildfire aerosol (Martinsson et al., 2022; Friberg et al., 2023) and
143 volcanic aerosol (Martinsson et al., 2025) and to obtain the AOD without influence from
144 attenuation.

145 ***2.2 Estimation of the stratospheric background***

146 The stratospheric aerosol background can rarely be observed in the entire stratosphere.
147 The last time the stratosphere was practically unaffected by injections from volcanic
148 eruptions and wildfires for several years was a few years around the turn of the
149 millennium (Solomon et al., 2011). Still, we need to find means to estimate the
150 stratospheric background because we can estimate the lidar ratio of stratospheric
151 injections from volcanic eruptions and wildfires (presented in next section) but not for

152 the background aerosol. Injections from aerosol events seldom affect the entire
153 stratosphere. Therefore, parts of the stratosphere can be in background conditions
154 when other parts are affected by aerosol injections.

155 To study the background conditions, the stratosphere was subdivided into nine parts
156 spanned by three altitude layers: the lowermost stratosphere (LMS, from the
157 tropopause to the 380 K isentrope, where the latter was obtained from MERRA-2
158 pressures and temperatures), the shallow Brewer-Dobson branch (sBD, between
159 isentropes 380 and 470 K) and the deep Brewer-Dobson branch (dBD, from the 470 K
160 isentrope to 35 km altitude), and three latitude regions: the Southern extratropics
161 (latitudes -80 to -20°), the tropics (latitudes -20 to 20°) and the Northern extratropics
162 (latitudes 20 to 80°). Data were averaged over 8 days resulting in 46 observations per
163 year in each of the nine stratospheric parts. To estimate the background conditions in
164 this 17-year study, the averages of the three years with the lowest average
165 backscattering of each 8-day period were formed. For two of the nine stratospheric
166 parts, the tropical sBD and dBD, background conditions were rare, wherefore only the
167 two lowest years were used in these two stratospheric parts. The method applied
168 results in the minimum aerosol load observed during the 17-year period. This means
169 that in addition to the tropospheric aerosol and precursor gases entering the
170 stratosphere across the tropical tropopause in the large-scale stratospheric circulation,
171 phenomena such as the ATAL (Vernier et al., 2015) and other exchanges across the
172 extratropical tropopause are included in the background.

173 The extracted lowest 8-day values formed a seasonal pattern that was fitted by the sum
174 of a constant and a sinusoidal function. These fits were used to express the average
175 backscattering of the background aerosol in each of the nine stratospheric parts over
176 the 17 years spanned by CALIOP measurements. The average backscattering converts
177 to AOD when multiplied with the lidar ratio. The fitted background was subtracted from
178 the measured total backscattering to form the backscattering from volcanic eruptions
179 and wildfires. These background-subtracted average backscattering data were
180 converted to AOD via the lidar ratios obtained from individual aerosol events, as
181 described in the next section.

182 **2.3 Lidar ratio**

183 The lidar ratio of the aerosol from the strongest volcanic eruptions and wildfires in the
184 period studied was estimated based on methodology described in Martinsson et al.
185 (2022), where individual dense aerosol layers are investigated. In that method a target
186 value in scattering ratio (R) obtained horizontally beside the studied aerosol layer (R_T) is
187 reached below the layer in an iterative procedure that results in an estimate of the
188 effective lidar ratio, while correcting for attenuation of the backscattered signal. The
189 effective lidar ratio obtained describes the average conditions of the entire layer where
190 the optical properties in principle can vary. However, the lidar ratio estimates are
191 obtained in dense aerosol layers, where the influence from background aerosol is small.

192 The uncertainty in the estimated lidar ratio depends on the AOD of the layer. A small
193 change in the lidar ratio (S) results in a substantial change in the scattering ratio (R)
194 below a dense layer, i.e., dS/dR is small for dense aerosol layers. dS/dR is obtained by
195 shifting R slightly around R_T . There is also an uncertainty in how well R_T represents the
196 aerosol beneath the layer. We estimate that uncertainty by the standard deviation of the
197 scattering ratio ($\sigma(R_T)$) obtained horizontally beside all the aerosol layers studied for
198 each volcanic eruption or wildfire. This is thus based on the assumption that the aerosol
199 horizontally beside and below the aerosol layer have the same standard deviation in R,
200 but the actual scattering ratios horizontally beside and below an individual layer are
201 uncorrelated. The estimated uncertainty becomes $dS/dR \times \sigma(R_T)$. Figure 1 shows all
202 $dS/dR \times \sigma(R_T)$ related to the AOD of all the estimations of the lidar ratio. The uncertainty in
203 the lidar ratio estimate increases as the layer AOD decreases, hence a limit was set to
204 $dS/dR \times \sigma(R_T) < 10$ sr to pass as a lidar ratio estimate. As a result, most estimates for
205 three volcanic eruptions, 2011 Nabro (Na11), 2014 Kelut (Ke14), and 2021 Soufriere
206 (So21), among the 12 eruptions and wildfires analyzed were lost, as illustrated in Figure
207 1.

208 For simplicity all the CALIOP data were evaluated using the standard lidar ratio of $S_0 =$
209 50 sr in the general evaluation. In the study of individual aerosol layers (Figure 1) both
210 the AOD based on the estimated lidar ratio and that based on S_0 were computed, where
211 the latter (AOD_{50}) was used to obtain the deviation caused by using S_0 . This deviation
212 depends on the S/S_0 ratio and AOD_{50} , where the effect of S/S_0 is the dominant one

213 except for very dense aerosol layers. The result from the general evaluation is corrected
214 afterwards based on the ratio of S_0 and the estimated S , see section 3.4.

215 **3. Results**

216 Here we will present the stratospheric aerosol from the tropopause to 35 km altitude
217 and the latitude range -80 to 80° in the era of lidar measurements by the CALIOP
218 instrument aboard the CALIPSO satellite. CALIOP measured the backscattered intensity
219 from a 532 nm laser beam, which can be converted to extinction by multiplying with the
220 ratio of extinction to backscatter, i.e. the lidar ratio. Knowing the lidar ratio thus is
221 central for quantification by obtaining AOD from CALIOP measurements. We developed
222 methodology to estimate the effective lidar ratio from CALIOP measurements, a
223 methodology that also corrects for attenuation of the laser signal (Martinsson et al.,
224 2022). Here we start by presenting the lidar ratio of the main aerosol events of the
225 CALIOP era before giving an overview of the AOD in the period studied. Then we
226 investigate separation of aerosol signals of aerosol events due to volcanic eruptions and
227 wildfires from signals due to stratospheric background aerosol. This is followed by
228 sections on corrections of AOD due to lidar ratio deviations from the commonly
229 assumed 50 sr, an overview of the AOD and a simplified estimate of the stratospheric
230 aerosol's radiative impact.

231 **3.1 Lidar ratio**

232 The main aerosol events affecting the stratosphere in the CALIOP era are presented in
233 Table 1. The methodology we use to estimate lidar ratios requires sufficiently dense
234 aerosol layers as described in section 2, implying that some of the events mentioned in
235 Table 1 are not suitable for the methodology. The lidar ratio was investigated for
236 stratospheric aerosol from nine volcanic eruptions and three wildfire events (Figure 2).
237 For some of these aerosol events the screening related to the uncertainty in the
238 estimated lidar ratio (Figure 1) resulted in few observations, namely for the 2011 Nabro,
239 2014 Kelut and the 2021 Soufriere eruptions. Most of the eruptions and wildfires display
240 a stable lidar ratio during the first month, whereas two of the events show an initial

241 decrease of the lidar ratio, the 2017 North American wildfire (Figure 2g) and the 2022
242 Hunga Ha'apai eruption (Figure 2l), towards a stable value.

243 Effective lidar ratios are presented here which are best suited for application to
244 measurements that, like CALIOP, are affected by multiple scattering (Martinsson et al.,
245 2022). Compared with previous estimates, the results presented here are approximately
246 20% lower than those of Prata et al. (2017) for the Kasatochi, Sarychev and Puyehue-
247 Cordon Caulle eruptions, who estimated lidar ratio for measurements that are not
248 affected by multiple scattering. Ohneiser et al. (2020) present Raman lidar measurements of
249 the 2019 Australian wildfire (Table 1) that are not affected by multiple scattering. On 2020-01-09
250 around 04:00 UTC (longitude -70.9, latitude -53.2) $S = 76$ sr was obtained. The closest CALIOP
251 measurement in space and time that we evaluated was taken on the same day at 04:05,
252 position (-43.4, -53.1) with $S = 75$ sr. The day before, at position (-57.2, -50.0) $S = 70$ sr and the
253 day after at position (-55.0, -57.1) $S = 71$ sr. All these three measurements belong to the fires
254 taking place last days of 2019, category B (outside the vortex) and are the three highest effective
255 lidar ratios obtained in this category.

256 Stratospheric aerosol resulting from most volcanic eruptions and wildfires have a lidar
257 ratio close to 50 sr, which is the commonly used lidar ratio for CALIOP data (Kar et al.,
258 2019). Notable exceptions with lidar ratio deviating by more than 5% from 50 sr are the
259 ash-dominated 2011 eruption of Puyehue-Cordón Caulle (Figure 2c), the 2019 Raikoke
260 eruption (Figure 2h) and the Australian wildfire in the last days of 2019 (Figure 2i). Also,
261 the 2011 Nabro eruption (Figure 2d) tends to deviate from the commonly adopted lidar
262 ratio of 50 sr of stratospheric aerosol, however the observations are too few for a firm
263 conclusion. In the forthcoming presentation the lidar ratio of 50 sr will be used before
264 the influence from deviations is addressed in sections 3.4 and 3.5.

265 **3.2 Stratospheric aerosol events overview**

266 At least 15 volcanic eruptions and 5 wildfires clearly affected the stratospheric aerosol
267 in the CALIOP era (Table 1). The latitude distribution of the stratospheric aerosol from
268 the tropopause to 35 km altitude is shown in Figure 3, and subdivided into three layers,
269 dBD, sBD, and LMS, in Figure 4 with full size versions in supplementary Figures S1 – S3.
270 Additionally, the altitude distribution is shown in three latitude ranges (-80 to -20°, -20 to
271 20° and 20 to 80°) in Figure 5 (supplementary Figures S4 – S6).

272 The influence from injections of aerosol from volcanic eruptions and wildfires has
273 durations of a few months to several years (Friberg et al., 2018). The latter category is
274 the aerosol events that enter the dBD branch in the tropics. The outstanding event
275 fulfilling this requirement in the period studied is the submarine eruption of Hunga
276 Ha'apai in 2022 (Figures 4a and 5a, b) where intense volcanism – sea interaction
277 (Seabrook et al., 2023; Mastin et al., 2024) formed large quantities of stratospheric
278 aerosol, whereas aerosol formation from SO₂ could explain only ~30% of the AOD
279 (Martinsson et al., 2025). The remaining aerosol events in the dBD have much lower
280 AODs. The Kelut eruption in 2014 affected the dBD for approximately 4 years. The
281 combined effect of the 2006 eruptions of Soufriere Hills and Rabaul (Figure 5b) show
282 similar long-term effects on the dBD in the tropics (Figure 4a). The combined effects of
283 4 volcanic eruptions, the 2018 Ambae, the two 2019 Ulawun and the 2021 Soufriere
284 eruptions, gradually increased the dBD aerosol load in the tropics. In addition to these
285 tropical eruptions, some extratropical aerosol events affected the dBD: the 2015
286 Calbuco eruption and some plumes injected above the main aerosol layer of the 2019
287 Raikoke eruption. Three wildfires also contributed aerosol to the extratropical dBD, the
288 2009 Australian, the 2017 Canada/USA and the 2019 Australian wildfires. The aerosol
289 from the latter fire formed a vortex where the aerosol rose above 31 km altitude (Kablick
290 et al., 2020). The extratropical aerosol events leave the dBD faster than the tropical ones
291 because of the extratropical downward motion of the BD circulation.

292 The shallow Brewer-Dobson (sBD) branch (Figure 4b) displays no such strong aerosol
293 event as the effect of the 2022 Hunga Ha'apai eruption on the dBD (Figure 4a). On the
294 other hand, many events had intermediate or small impacts. The Australian wildfires at
295 the end of 2019 and the beginning of 2020 made an initial strong impact that was rapidly
296 reduced by loss of 90% of the aerosol with a half-life of 10 days, likely due to photolysis
297 of organic aerosol (Friberg et al., 2023), as did the 2017 North American wildfire but with
298 a lower aerosol load (Martinsson et al. 2022) and, to a still lower extent, the 2009
299 Australian wildfire. The main volcanic eruptions affecting the sBD branch were the 2008
300 Kasatochi, 2009 Sarychev, 2011 Nabro, 2015 Calbuco, 2019 Raikoke and, after a delay
301 due to transport from the dBD branch, the 2022 Hunga Ha'apai eruptions (Figure 4a, b).
302 Other volcanos with smaller impact on the sBD branch were the 2006 Soufriere Hills

303 and Rabaul, the 2010 Merapi, 2014 Kelut, 2018 Ambae, 2019 Ulawun (2 eruptions) and
304 2021 Soufriere eruptions.

305 The LMS (Figure 4c), the last stratospheric part passed by the air and its trace
306 substances in the large-scale stratospheric circulation before exiting to the
307 troposphere, is affected by all stratospheric aerosol events. In addition, some
308 extratropical aerosol events do not reach beyond the LMS. The Kasatochi eruption
309 resulted in two distinct aerosol layers, a thin layer in the sBD whereas the main part of
310 its effluents was injected both sides of and close to the tropopause (Andersson et al.,
311 2015). Other exclusive LMS events in the period studied here are the 2011 Puyehue-
312 Cordón Caulle eruption and the 2006 Australia wildfire.

313 Most volcanic eruptions show a gradual increase in AOD over few months before
314 reaching its maximum because of the time required for aerosol dynamical processing
315 and to transform sulfur dioxide into sulfate, which usually is the main component of the
316 aerosol from volcanic eruptions. Notable exceptions are the 2022 Hunga Ha'apai and
317 the 2011 Puyehue-Cordón Caulle eruptions (Figure 3). The aerosol of the latter eruption
318 mainly consisted of volcanic ash (Vernier et al., 2013) and the former by aerosol
319 containing sulfate and sea-salt from volcanism – sea interaction (Martinsson et al.,
320 2025). These eruptions are thus less influenced by delay in aerosol formation from
321 chemical transformation. The wildfires in the years 2009, 2017, 2019 and 2020 also
322 rapidly reach the maximum AOD before a decline due to photolysis of organic
323 compounds reduces the AOD by 90% (Martinsson et al., 2022; Friberg et al., 2023).

324 ***3.3 Stratospheric background***

325 The stratospheric background aerosol is not a well-defined concept. One way is to
326 include all but major aerosol events in the background to obtain a persistently variable
327 background (Solomon et al., 2011). An alternative background is based on SAGE II
328 measurements in the volcanically quiescent period in the late 1990s to early 2000s
329 (Kremser et al., 2016). CALIOP measurements were not available in those years. A
330 volcanic eruption or wildfire rarely affects the entire stratosphere. Therefore, we divided
331 the stratosphere into nine sections by altitude and latitude thereby increasing the
332 probability of finding conditions close to background separately in each of the layers

333 using the average of the three lowest average backscattering values (in two cases the
334 two lowest) of each layer over the year (Figure 6), as described in the methods section.

335 The distribution of aerosol over the nine layers used to extract the background aerosol is
336 shown in Table 2. Seven of the nine layers each contain 11 – 15% of the background
337 aerosol in the stratosphere from the tropopause to 35 km altitude during conditions that
338 are close to background. The smallest contribution comes from the tropical LMS, which
339 is to be expected given the small air volume of that layer. The tropical sBD also has a
340 small contribution, but that cannot be explained by the air volume. This layer where
341 tropospheric air enters the stratosphere extends to approximately 20 km altitude, where
342 UV radiation intensity is too weak to efficiently oxidize carbonyl sulfide (Weisenstein et
343 al., 1997), which is an important precursor gas of the stratospheric background aerosol
344 (Crutzen, 1976; Kremser et al., 2016), a topic we return to below. Seasonal changes in
345 aerosol background average backscattering are most pronounced in the extratropical
346 LMS, especially in the NH. The volume of LMS varies over the year. That variation
347 (Appenzeller et al., 1996) approximately coincides with the variation in Figure 6 both in
348 terms of seasonality and the stronger amplitude in the LMS of the NH. The seasonal
349 variation of background backscattering in the LMS therefore likely reflects both the seasonal
350 variation of LMS volume and true variability in aerosol loading. Poleward transport in the BD
351 circulation maximizes in the winter resulting in increased extratropical downward
352 motion of the stratospheric aerosol layer in the spring resulting in low aerosol load in the
353 summer LMS when the mass transport across its upper boundary is at its minimum. The
354 latter also coincides with the weakening of the subtropical Jetstream which increases
355 the tropospheric influence on the LMS. In the summer/early fall there is also influence
356 from ATAL (Vernier et al., 2015) and small wildfires briefly affecting the stratosphere
357 (Peterson et al., 2025). The chemical composition of the LMS aerosol of the Northern
358 hemisphere in that period differs from winter/spring/early summer by having a larger
359 carbon than sulfur content (Martinsson et al., 2019). The change in composition can be
360 caused by the ATAL and/or small wildfires which thus contribute to the effect of the
361 large-scale stratospheric circulation in the build-up of the NH LMS aerosol load during
362 late summer and fall.

363 The average backscattering of the stratospheric aerosol and the estimated background
364 (Figure 6) in nine altitude and latitude layers is shown in Figure 7. By comparing these
365 two quantities, we verify the underlying assumption in the method used to obtain the
366 background that the stratospheric aerosol background has no long-term trend, which
367 agrees with previous observations (Kremser et al., 2016). Subtracting the background,
368 we obtain the average backscattering from volcanic eruptions and wildfires. The net
369 average backscattering of the layers was converted to AOD of the layers by
370 multiplication with the lidar ratio of 50 sr in Figure S8 with contributions from volcanic
371 eruptions and wildfires as described in section 3.2.

372 Except for a tiny peak in the LMS in the Northern extratropics, 2013 is close to
373 background conditions (Figure 7). The stratospheric background aerosol is often
374 thought of as a layer located above 20 km altitude in the tropics and lower in the
375 extratropics. This is approximately true in terms of scattering ratio (R), the optical
376 equivalent of mixing ratio (Figure 8a). More than half of the air entering the tropical
377 stratosphere is transported polewards in the sBD (Lin and Fu, 2013), where the
378 scattering ratio remains low in a band closest to the tropopause (Figure 8a). This band
379 contains young stratospheric air compared to air at the same altitude but at higher
380 latitude (Austin and Li, 2006; Butchart, 2014; Ploeger et al., 2021). In the air rising
381 further in the tropical stratosphere a dramatic increase of the aerosol mixing ratio can
382 be seen above 20 km altitude. The aerosol signal increases by a factor of 2.5 (Figure 8b)
383 from 19 to 25 km altitude in the latitude range -10 to 10°, i.e., 70% of the aerosol at 25
384 km is formed above 19 km altitude. The dBD air is transported polewards and descends
385 at higher latitudes than the sBD air (Figure 8a). With a typical vertical velocity of 20
386 m/day (Mote et al., 1998) the transport from the tropical tropopause (at 17 km) to 19 km
387 altitude requires approximately 100 days, providing ample time for conversion of SO₂
388 before reaching the latter altitude (Nicknish et al., 2025). Hence, little SO₂ enters the
389 dBD, implying particle formation from another source. Intensifying UV radiation with
390 altitude causes oxidation of the most abundant sulfur compound in the atmosphere,
391 i.e., carbonyl sulfide (OCS) (Crutzen, 1976; Kremser et al., 2016), whereas this
392 compound remains intact in the sBD. The requirement of intense UV radiation for
393 oxidation makes OCS an important aerosol formation pathway mainly in the dBD. The

394 formed aerosol is transported polewards where downward transport brings the aerosol
395 to the sBD and LMS layers before the transport out of the stratosphere (Figure 8a). The
396 formation pathways of the stratospheric background aerosol are still debated. The
397 estimated contribution of OCS to the stratospheric background aerosol ranges from 20
398 – 50% (Sheng et al., 2015; Chin and Davies, 1995) to 70% or more (Crutzen, 1976; Brühl
399 et al., 2012). High-resolution lidar data, like that of CALIOP, can be used to constrain
400 modeling efforts to quantify sulfurous aerosol sources by reconstructing the CALIOP
401 observations in Figure 8 to understand the sources of the background aerosol.

402 When we instead consider the absolute background aerosol load (Figure 8c) we find the
403 highest aerosol load at low stratospheric altitudes. The air in the Brewer-Dobson
404 circulation becomes compressed during the downwelling in the extratropics in
405 accordance with the altitude-dependence of the atmospheric pressure. Mixing across
406 the extratropical tropopause culminating in the late summer with the ATAL affects the
407 aerosol load in the LMS but does not affect the mixing ratios appreciably (Figure 8a).
408 However, somewhat higher scattering ratios are found in the ATAL region (15 – 45° N and
409 13 – 18 km altitude (Vernier et al., 2015)) compared with the same region of the
410 southern hemisphere. In monthly resolution, rather than the yearly resolution of Figure
411 8, enhanced aerosol load in the ATAL area is clearly visible in July – September 2013
412 (Martinsson et al., 2017). During background conditions approximately 60% of the
413 aerosol backscattering signal (AOD divided by the lidar ratio) is found in the two lower
414 layers, sBD and LMS (Table 2), containing aerosol transported from both the sBD and
415 dBD of the tropics.

416 **3.4 Correction of lidar ratio**

417 Thus far we have presented AODs with the lidar ratio set to 50 sr. The lidar ratios of the
418 individual measurements are shown in Figure 2. In Figure 9a we show the averages with
419 statistical uncertainty (standard error and double-sided 95% confidence interval). As
420 already pointed out, three of the eruptions (Nabro 2011, Kelut 2014 and Soufriere 2021)
421 cannot be evaluated statistically due to few available measurements. Most of the
422 aerosol events show effective lidar ratios of approximately 50 sr, whereas the aerosol
423 from Puyehue-Cordón Caulle (2011), Raikoke (2019) and the Australian wildfires in the
424 end of 2019 deviates from 50 sr by more than 5%.

425 To convert the AOD obtained using $S_0 = 50$ sr to the estimated lidar ratio (S) we need to
426 consider the linear dependence of the AOD on the lidar ratio. A secondary effect relates
427 to the level of AOD. For the latter, we need to evaluate the occurrence of dense aerosol
428 layers. All the measurements fulfilling the criteria on uncertainty of the lidar ratio
429 estimate (Figure 1) are displayed in Figure 9b. Initially layer AODs sometimes exceed 1.
430 After 20 days the AOD of the individual aerosol layers is mostly 0.25 and lower, except
431 for the 2019 Australian wildfire that remain somewhat higher probably due to less air
432 mixing in the vortex formed (Kablick et al., 2020). We corrected the AODs by S/S_0 for
433 volcanic eruptions and wildfires that formed an aerosol with effective lidar ratio
434 deviating more than 5% from $S_0 = 50$ sr, whereas the residual correction connected with
435 the AOD of an aerosol layer was not accounted for (see the methods section for further
436 detail) because the effect is small (Figure 9c). In the general evaluation we did not
437 separate the aerosol backscattering from the 2019 and 2020 Australian wildfires that
438 were only a few days apart. The 2020 fire was dominant in terms of AOD with 80 – 90%
439 of the total AOD from the two fires (Friberg et al., 2023). Here, we weigh the lidar ratios
440 of the two fires accordingly to obtain $S = 53.3$ representing both fires.

441 The blue dots in Figure 10a over the stratospheric AOD were corrected for deviant lidar
442 ratios in 2011 (Puyehue-Cordón Caulle eruption by +8%) and 2019 – 2020 (Raikoke
443 eruption by -12% and Australian wildfires by +7%). The corresponding AOD using $S_0 = 50$
444 sr is represented by a thin gray line showing that the AOD was practically not affected by
445 the correction in 2011 because that year was dominated by aerosol from another
446 eruption (Nabro, Figure 3). The AOD from the Raikoke (2019) eruption shifted down
447 slightly by the correction, and that of the 2019 – 2020 Australian wildfires shifted
448 upwards.

449 Altogether the changes in AOD from the corrections due to deviant lidar ratio were
450 found to be minor, the largest correction (-12%) was applied to the AOD of the Raikoke
451 eruption. However, we could not statistically quantify all major aerosol events, most
452 notably the Nabro eruption in 2011 (Figure 2). Our results show that assumption of an
453 effective lidar ratio of 50 sr works satisfactory in most cases in the 17-year period
454 studied when the stratospheric aerosol is influenced by volcanism or wildfires. The

455 applied method to obtain the effective lidar ratio cannot be used for optically thin layers
456 like the background aerosol.

457 **3.5 AOD of stratospheric aerosol events**

458 The AOD from aerosol events were approximately evenly distributed over the three
459 latitude regions (-80 to -20°, -20 to 20° and 20 to 80°) studied (Table 2). The altitude
460 distribution showed most influence from volcanic eruptions and wildfires in the sBD
461 (43%), followed by the dBD (31%), and the often overlooked LMS (Andersson et al.,
462 2015) held 26% of the AOD from aerosol events in the period 2006 – 2023.

463 The average stratospheric AOD, with the contribution from background aerosol
464 subtracted, from the tropopause to 35 km altitude in the latitude range -80 to 80° is
465 shown in Figure 10a. The intense volcanism – sea interaction of the Hunga Ha’apai
466 eruption in the beginning of 2022 (Martinsson et al., 2025) resulted in the highest and
467 broadest AOD peak (Figure 10a). Other prominent events were the Australian wildfires
468 at the end of 2019 and the beginning of 2020, the eruptions of Raikoke (2019), Sarychev
469 (2009), Nabro (2011), Calbuco (2015) and Kasatochi (2008) affecting the stratospheric
470 AOD together with several eruptions and wildfires having smaller contributions (Table
471 1).

472 The average influence of volcanic eruptions and wildfires each year is shown in Figure
473 10b. The most affected year was 2022 with an average AOD of 0.01 from aerosol events.
474 That year is likely followed by 2023, for which we have no data from the second half of
475 the year. Both these years were mainly affected by the 2022 Hunga Ha’apai eruption.
476 Then follows 2020 (mainly the 2019-20 Australian wildfires with some contribution from
477 the Raikoke eruption) with background-subtracted AOD of 0.006, 2009 (Sarychev) and
478 2019 (Raikoke) both years with AOD of 0.005, whereas 2011 (mainly Nabro) reach AOD
479 from aerosol events of almost 0.004. The average background-subtracted AOD from
480 volcanic eruptions and wildfires from 2006 to 2023 is 0.0031. The background aerosol
481 produces global average backscattering of 0.00011 sr^{-1} , which, with the commonly used
482 assumption of a lidar ratio of 50 sr, corresponds to a stratospheric background AOD of
483 0.0057.

484 The yearly average AOD from aerosol events ranges from 0.0002 (in 2013) to 0.010
485 (2022) and the average over the 17 years studied is 0.0031. Making use of previous
486 estimates of the relation between radiative forcing (F) and stratospheric AOD ($F = -$
487 $24 \times \text{AOD}$ in W/m^2) (Schmidt et al., 2018), we can obtain a first, simplified estimate of the
488 radiative effect of the stratospheric aerosol events. This relation is based on volcanic
489 sulfate aerosol, which is the dominant type of stratospheric aerosol event in the 17-year
490 period studied. The relation is not designed to deal with absorbing wildfire aerosol,
491 which cause uncertainty in the average radiative forcing of the period estimated here.
492 This simplified, order-of-magnitude estimate of the global stratospheric yearly average
493 total effective radiative forcing due to volcanic eruptions and wildfires varies between -
494 0.006 and -0.24 W/m^2 , with the average -0.074 W/m^2 in the period 2006 to 2023.
495 Assuming a lidar ratio of 50 sr, the stratospheric background aerosol effective radiative
496 forcing becomes -0.14 W/m^2 .

497 **4. Discussion**

498 Stratospheric aerosol optical properties are often described using solar occultation
499 data, especially from the 22 years of SAGE II measurements (Bauman et al., 2003;
500 Thomason et al., 2018). Prior comparisons of CALIOP lidar-based results with solar
501 occultation (SAGE III/ISS) show agreement within approximately 10% in the latitude
502 range -30 to 30° and increasing discrepancy at midlatitudes reaching above 50% at high
503 latitudes for background aerosol in the altitude range 20 – 30 km (Kar et al., 2019), and
504 discrepancies exceeding 50% is reported at altitudes below 17 km (Kovilakam et al.,
505 2023). The main reason for these differences was attributed to the unknown lidar ratio
506 of CALIOP (Kar et al., 2019; Kovilakam et al., 2023). Here we have estimated the CALIOP
507 effective lidar ratio of the aerosol from several volcanic eruptions and wildfires (Figure
508 2), and in Figure 9d the latitude distribution of the estimates is shown. Using the
509 standard lidar ratio of 50 sr cannot explain the latitude- and altitude-dependence in the
510 lidar – solar occultation comparison obtained in Kar et al. (2019) and Kovilakam et al.
511 (2023) for aerosol from volcanic eruptions and wildfires in the CALIOP era.

512 The latitude-dependent discrepancy at 532 nm wavelength between SAGE III/ISS and
513 CALIOP at high altitudes in the period June 2017 to August 2018 above 20 km (, i.e.,

514 essentially in the dBD) reported by Kar et al. (2019) concerns a period when the dBD
515 was close to background (Figure 7). The method used here for estimating the lidar ratio
516 does not work for background conditions (Figure 1). Using the standard CALIOP lidar
517 ratio for the background aerosol (50 sr) results in the global average background AOD of
518 0.0057. SAGE II measurements during the volcanically quiescent period 1998 – 2000
519 resulted in AOD of 0.0040 (estimated from Solomon et al. (2011), their Figure 2), who
520 integrated the stratospheric AOD from 15 km altitude. When removing the stratospheric
521 aerosol data below 15 km from the CALIOP measurements, the stratospheric
522 background AOD is reduced by 31% to 0.0039 using lidar ratio 50 sr. This is almost
523 identical to the background AOD reported in Solomon et al. (2011), thus indicating that
524 the stratospheric background aerosol on average has a lidar ratio close to 50 sr. Kar et
525 al. (2019) found that aerosol backscattering during background conditions at altitudes
526 above 20 km in the extratropics should be converted to AOD by a variable lidar ratio.
527 Mid- and high-latitude air in this altitude range has a high stratospheric age (~5 years)
528 (Ploeger et al., 2021), implying that particle gravitational settling has long time to affect
529 the particle size distribution, and hence the optical properties of the aerosol. In Figure
530 8c we find most of the aerosol above 20 km altitude to be located in the tropics,
531 implying that the deviations at high latitudes that Kar et al. (2019) reported have little
532 impact on global AOD, and thus little impact on our comparison with Solomon et al.
533 (2011) that deals with the entire stratosphere above 15 km altitude.

534 In a comparison by Kovilakam et al. (2023) between CALIOP and SAGE III/ISS during
535 November 2017, 2 – 3 months after the Canada/USA fire (Table 1) large deviations were
536 found at high latitudes and altitudes as in Kar et al. (2019), as described above.
537 Kovilakam et al. (2023) also found large differences in the densest part of the
538 stratosphere, i.e., at altitudes below 17 km. In GloSSAC the more than 50% lower values
539 of limb-viewing techniques (SAGE and OSIRIS) than CALIOP were adopted, justified by
540 citing uncertainties in the lidar ratio to discard CALIOP results at low altitudes
541 (Kovilakam et al., 2023).

542 The main advantages of solar occultation measurements are that extinction is
543 measured and that several wavelengths are available. Lidar measurements also have
544 some distinct advantages. Lidars with nadir view have several hundred kilometers

545 shorter measurement path enabling measurements in dense aerosol layers (Martinsson
546 et al., 2022, their Figure 7) producing viable, quantitative results when limb views fail,
547 provided that the lidar ratio is known. The lidar vertical resolution is superior and is not
548 relying on assumptions on homogeneity of the aerosol layer measured, like solar
549 occultation measurements do (Damadeo et al., 2013). Accurate altitude descriptions
550 with high vertical resolution of stratospheric injections (Sandvik et al., 2021) are vital for
551 the outcome of stratospheric aerosol modeling (Axebrink et al., 2025). Relying on these
552 points we argue that the role of lidar measurements should be re-evaluated. Existing
553 methods differ in their sensitivity to aerosol properties and in their temporal coverage.
554 We need to take advantage of the best qualities of all available methods, both in terms
555 of physical properties and time coverage. Re-evaluation of CALIOP data could improve
556 stratospheric aerosol climatologies, like GloSSAC (Thomason et al., 2018, Kovilakam et
557 al., 2020; Kovilakam et al., 2023), that are designed for the modeling community,
558 ultimately leading to a better representation of the stratospheric aerosol in climate
559 modeling.

560 Hopefully the lidar ratio of stratospheric aerosol can be further clarified when the
561 aerosol load is close to background conditions by lidar systems measuring both
562 backscattering and extinction. The ATLID aboard the EarthCARE satellite (Illingworth et
563 al., 2015) that started to produce data in July 2024 and the NASA and Italian Space
564 Agency collaboration on the 3 wavelength lidar CALIGOLA planned for launch in the
565 early 2030s (Behrenfeld et al., 2023) are future means to further clarify extinction
566 obtained from lidars, and to optimally combine solar occultation and lidar
567 measurements for future long-term records on the optical properties of the
568 stratospheric aerosol with high and unambiguous vertical resolution.

569 **5. Conclusions**

570 The entire backscattering record at 532 nm wavelength of the satellite-based lidar
571 system CALIOP spanning years 2006 to 2023 was investigated in this study. During this
572 period injections of aerosol and precursor gases into the stratosphere of 15 volcanic
573 eruptions and 5 wildfires were identified. The effective lidar ratios of 12 volcanic
574 eruptions and wildfires were investigated to convert the measured backscattering to

575 extinction. The measurements were evaluated and corrected for attenuation using the
576 lidar ratio $S_0 = 50$ sr. The aerosol events having a lidar ratio deviating by more than 5%
577 from S_0 were corrected after the general evaluation.

578 Background aerosol conditions are more likely to occur in sublayers than throughout
579 the entire stratosphere. The stratosphere was therefore subdivided into 9 layers
580 spanned by altitude (lowermost stratosphere (LMS), shallow Brewer-Dobson branch
581 (sBD), deep Brewer-Dobson branch (dBD)) and latitude intervals (tropics and Southern
582 and Northern extratropics). The estimated backgrounds of layers were combined to
583 obtain the background aerosol of the entire stratosphere. The backscattering of
584 background aerosol was converted to aerosol optical depth (AOD) using a lidar ratio of
585 50 sr. That AOD agrees well with measurements with solar occultation (SAGE II) during
586 1998 – 2000 in the volcanically quiescent period. The average backscattering of seven of
587 the nine layers each contains 11 - 15% of the entire background aerosol. The tropical
588 LMS has a small contribution due to very small volume compared to the other layers.
589 The tropical sBD was also clearly lower (7%) because oxidation of carbonyl sulfide
590 (OCS) occurs at higher altitudes in the upwards moving air in the tropical stratosphere.
591 We find that 70% of the aerosol in the tropical dBD is formed above 19 km altitude
592 during background conditions, due to formation from OCS. A several kilometers thick
593 band of low aerosol load directly above the tropopause was identified which we
594 attribute to young stratospheric air transported in the sBD. Above that layer a broad
595 band with high aerosol load was found which we identify as the tropical dBD air that is
596 transported polewards and downwards resulting in high aerosol load in the sBD and
597 LMS at mid and high latitudes. Considering the ongoing debate on the sources of
598 stratospheric background aerosol, these highly resolved CALIOP data could be useful to
599 constrain modeling efforts on the sources of the stratospheric sulfurous aerosol.

600 The background aerosol AOD (0.0057) was subtracted from the measurements to
601 obtain the influence from aerosol and trace gas injections into the stratosphere. The
602 most important aerosol events in the 17-year period are the 2022 Hunga Ha'apai
603 eruption and the Australian wildfires (2019-20) followed by the volcanic eruptions
604 Raikoke (2019), Sarychev (2009) and Nabro (2011). The global yearly average AOD
605 increase from volcanic and wildfire injections spans 0 to 0.010.

606 Limb-viewing solar occultation measurements have some distinctive advantages in that
607 much of the early measurements in the satellite era were undertaken with that method.
608 They also deliver direct measurements of extinction, and at several wavelengths. Here,
609 we have estimated the effective lidar ratio of the CALIOP measurements to obtain
610 extinction from backscattering measurements. Lidars operating in nadir view, like
611 CALIOP, have several hundred kilometers (or a factor of more than 100) shorter
612 measurement path than limb-viewers, allowing measurements in dense aerosol layers
613 where limb-viewers fail. Lidars have unambiguous and superior vertical resolution over
614 other satellite instruments providing models with important input on aerosol and trace
615 gas injections into the stratosphere. Newer lidars that measure extinction are launched,
616 under construction and planned. Future work should better reconcile lidar and solar
617 occultation records and exploit their complementary strengths. With known effective lidar
618 ratios the relation between CALIOP and solar occultation measurements needs to be
619 re-evaluated, especially in the dense stratospheric air located below 17 km altitude in
620 long-term records over the optical properties of the stratospheric aerosol.

621 *Data availability.* The data used are publicly available: CALIOP V4.51 lidar data
622 (<https://search.earthdata.nasa.gov/search?fp=CALIPSO>).

623 *Author contributions.* BGM planned the study, undertook most of the data analysis and
624 wrote the paper. JF participated in the planning of the study, undertook part of the data
625 analysis and MKS contributed. JF and MKS undertook data extraction and handling for
626 the data analysis. All authors participated in discussions and commented on the
627 manuscript.

628 *Competing interests.* The contact author and the co-authors declare that they have no
629 competing interests.

630 *Acknowledgements.* Aerosol products from the CALIOP sensor were produced by NASA
631 Langley Research Center.

632 *Financial support.* The Swedish National Space Agency, contracts 2025-00200 and
633 2022-00157, Johan Friberg. The Crafoord Foundation, contract 20240901, Johan Friberg.
634 Formas, contract 2025-01869, Johan Friberg. Formas, contract 2020-00997, Moa
635 Sporre. The Swedish Research Council 2022-02836, Moa Sporre.

636 **References**

- 637 Andersson, S. M., Martinsson, B. G., Friberg, J., Brenninkmeijer, C. A. M., Rauthe-
638 Schöch, A., Hermann, M., van Velthoven, P. F. J., and Zahn, A.: Composition and
639 evolution of volcanic aerosol from eruptions of Kasatochi, Sarychev and
640 Eyjafjallajökull in 2008–2010 based on CARIBIC observations, *Atmos. Chem.*
641 *Phys.*, 13, 1781–1796, <https://doi.org/10.5194/acp-13-1781-2013>, 2013.
- 642 Andersson, S. M., Martinsson, B. G., Vernier, J.-P., Friberg, J., Brenninkmeijer, C. A. M.,
643 Hermann, M., van Velthoven, P. F. J., and Zahn, A.: Significant radiative impact of
644 volcanic aerosol in the lowermost stratosphere, *Nat. Commun.*, 6, 1–8,
645 <https://doi.org/10.1038/ncomms8692>, 2015.
- 646 Appenzeller, C., Holton, J.R., and Rosenlov, K.H.: Seasonal variation of mass transport
647 across the tropopause, *J. Geophys. Res.* 101, 15071-15078, 1996.
- 648 Austin, J., and Li, F.: On the relationship between the strength of the Brewer-Dobson
649 circulation and the age of stratospheric air, *Geophys. Res. Lett.*, 33, L17807,
650 [doi:10.1029/2006GL026867](https://doi.org/10.1029/2006GL026867), 2006.
- 651 Axebrink, E., Sporre, M.K., and Friberg, J.: Impact of SO₂ injection profiles on simulated
652 volcanic forcing for the 2009 Sarychev eruptions– investigating the importance of
653 using high-vertical-resolution methods when compiling SO₂ data, *Atmos. Chem.*
654 *Phys.*, 25, 2047–2059, <https://doi.org/10.5194/acp-25-2047-2025>, 2025.
- 655 Baars, H., Ansmann, A., Ohneiser, K., Haarig, M., Engelmann, R., Althausen, D.,
656 Hanssen, I., Gausa, M., Pietruczuk, A., Szkop, A., Stachlewska, I. S., Wang, D.,
657 Reichardt, J., Skupin, A., Mattis, I., Trickl, T., Vogelmann, H., Navas-Guzmán, F.,
658 Haeferle, A., Acheson, K., Ruth, A. A., Tatarov, B., Müller, D., Hu, Q., Podvin, T.,
659 Goloub, P., Veselovskii, I., Pietras, C., Haeffelin, M., Fréville, P., Sicard, M.,
660 Comerón, A., Fernández García, A. J., Molero Menéndez, F., Córdoba-Jabonero,
661 C., Guerrero-Rascado, J. L., Alados-Arboledas, L., Bortoli, D., Costa, M. J.,
662 Dionisi, D., Liberti, G. L., Wang, X., Sannino, A., Papagiannopoulou, N., Boselli,
663 A., Mona, L., D’Amico, G., Romano, S., Perrone, M. R., Belegante, L., Nicolae, D.,
664 Grigorov, I., Gialitaki, A., Amiridis, V., Soupion, O., Papayannis, A., Mamouri, R.-
665 E., Nisantzi, A., Heese, B., Hofer, J., Schechner, Y. Y., Wandinger, U., and
666 Pappalardo, G.: The unprecedented 2017–2018 stratospheric smoke event:
667 decay phase and aerosol properties observed with the EARLINET, *Atmos. Chem.*
668 *Phys.*, 19, 15183–15198, <https://doi.org/10.5194/acp-19-15183-2019>, 2019.
- 669 Bauman, J. J., Russell, P. B., Geller, M. A., and Hamill, P.: A stratospheric aerosol
670 climatology from SAGE II and CLAES measurements: 2. Results and
671 comparisons, 1984–1999, *J. Geophys. Res.*, 108, 4383,
672 <https://doi.org/10.1029/2002JD002993>, 2003.
- 673 Behrenfeld, M.J., Lorenzoni, L., Hu, Y., Bissom, K.M., Hostetler, C.A., Di Girolamo, P.,
674 Dionisi, D., Longo, F., and Zoffoli, S.: Satellite Lidar Measurements as a Critical
675 New Global Ocean Climate Record, *Remote Sens.* 15, 5567. <https://doi.org/10.3390/rs15235567>, 2023.

677 Brühl, C., Lelieveld, J., Crutzen, P.J., and Tost, H.: The role of carbonyl sulphide as a
678 source of stratospheric sulphate aerosol and its impact on climate, *Atmos.*
679 *Chem. Phys.*, 12, 1239–1253, www.atmos-chem-phys.net/12/1239/2012/
680 [doi:10.5194/acp-12-1239-2012](https://doi.org/10.5194/acp-12-1239-2012), 2012.

681 Butchart, N., The Brewer-Dobson circulation, *Rev. Geophys.*, 52, 157–184,
682 [doi:10.1002/2013RG000448](https://doi.org/10.1002/2013RG000448), 2014.

683 Carn, S.A., Krueger, A.J., Krotkov, N.A., Yang, K., and Evans, K.: Tracking volcanic sulfur
684 dioxide clouds for aviation hazard mitigation, *Nat Hazards*, 51, 325–343 DOI
685 10.1007/s11069-008-9228-4, 2009.

686 Carn, S.A., and Prata, F.J., Satellite-based constraints on explosive SO₂ release from
687 Soufrière Hills Volcano, Montserrat, *Geophys. Res. Lett.*, 37, 1-5, L00E22,
688 [doi:10.1029/2010GL044971](https://doi.org/10.1029/2010GL044971), 2010.

689 Carn, S. A., Krotkov, N. A., Fisher, B. L., and Li, C.: Out of the blue: Volcanic SO₂
690 emissions during the 2021–2022 eruptions of Hunga Tonga– Hunga Ha’apai
691 (Tonga), *Front. Earth Sci.*, 10, 976962,
692 <https://doi.org/10.3389/feart.2022.976962>, 2022.

693 Chin, M., and Davies, D.D.: A reanalysis of carbonyl sulfide as a source of stratospheric
694 background sulfur aerosol, *J. Geophys. Res.* 100, 8993-9005, 1995.

695 Clarisse, L., Hurtmans, D., Clerbaux, C., Hadji-Lazaro, J., Ngadi, Y., and Coheur, P.-F.:
696 Retrieval of sulphur dioxide from the infrared atmospheric sounding
697 interferometer (IASI), *Atmos. Meas. Tech.*, 5, 581–594,
698 <https://doi.org/10.5194/amt-5-581-2012>, 2012.

699 Clarisse, L., Coheur, P.-F., Prata F., Hadji-Lazaro, J., Hurtmans, D., and Clerbaux, C.: A
700 unified approach to infrared aerosol remote sensing and type specification,
701 *Atmos.Chem.Phys.*, 13, 2195–2221, www.atmos-chem-phys.net/13/2195/2013/
702 [doi:10.5194/acp-13-2195-2013](https://doi.org/10.5194/acp-13-2195-2013), 2013.

703 Crutzen, P.J.: The possible importance of CSO for the sulfate layer of the stratosphere,
704 *Geophys. Res. Lett.* 3, 73-76, 1976.

705 Cruz, M.G., Sullivan, A.L., Gould, J.S., Sims, N.C., Bannister, A.J., Hollis, J.J., and Hurley,
706 R.J.: Anatomy of a catastrophic wildfire: The Black Saturday Kilmore East fire in
707 Victoria, Australia, *Forest Ecol. Manag.* 284, 269-295, 2012.

708 Damadeo, R.P., Zawodny, J.M., Thomason, L.W., and Iyer, N.: SAGE version 7.0
709 algorithm: application to SAGE II, *Atmos. Meas. Tech.*, 6, 3539–3561,
710 www.atmos-meas-tech.net/6/3539/2013/, 2013.

711 Friberg, J., Martinsson, B. G., Andersson, S. M., Brenninkmeijer, C. A. M., Hermann, M.,
712 Van Velthoven, P. F. J., and Zahn, A.: Sources of increase in lowermost
713 stratospheric sulphurous and carbonaceous aerosol background concentrations

714 during 1999–2008 derived from CARIBIC flights, *Tellus B*, 66, 23428,
715 <https://doi.org/10.3402/tellusb.v66.23428>, 2014.

716 Friberg, J., Martinsson, B. G., Andersson, S. M., and Sandvik, O. S.: Volcanic impact on
717 the climate– the stratospheric aerosol load in the period 2006–2015, *Atmos.*
718 *Chem. Phys.*, 18, 11149–11169, <https://doi.org/10.5194/acp-18-11149-2018>,
719 2018.

720 Friberg, J., Martinsson, B. G., and Sporre, M. K.: Short- and long-term stratospheric
721 impact of smoke from the 2019–2020 Australian wildfires, *Atmos. Chem. Phys.*,
722 23, 12557–12570, <https://doi.org/10.5194/acp-23-12557-2023>, 2023.

723 Fromm, M., Lindsey, D. T., Servranckx, R., Yue, G., Trickl, T., Sica, R., Doucet, P., and
724 Godin-Beekmann, S.: The untold story of pyrocumulonimbus, *B. Am. Meteorol.*
725 *Soc.*, 91, 1193–1209, 2010.

726 Fromm, M., Kablick III, G. P., Peterson, D. A., Kahn, R. A., Flower, V. J. B., and Seftor, C. J.:
727 Quantifying the source term and uniqueness of the August 12, 2017 Pacific
728 Northwest pyroCb event, *J. Geophys. Res.*, 126, e2021JD034928,
729 <https://doi.org/10.1029/2021JD034928>, 2021.

730 Garofalo, L. A., Levin, E. J. T., Campos, T., Kreidenweis, S. N., and Farmer, D. K.:
731 Emission and evolution of submicron organic aerosol in smoke from wild fires in
732 the western United States, *ACS Space Chem.*, 3, 1237–1247, 2019.

733 Gelaro, R., McCarty, W., Suarez, M. J., Todling, R., Moloud, A., Takacs, L., Randles, C. A.,
734 Darmenov, A., Bosilovich, M. G., Reichle, R., Wargan, K., Coy, L., Cullather, R.,
735 Draper, C., Akella, S., Buchard, V., Conaty, A., da Silva, A. M., Gu, W., Kim, G.-K.,
736 Koster, R., Lucchesi, R., Merkova, D., Nielsen, J. E., Partyka, G., Pawson, S.,
737 Putman, W., Rienecker, M., Schubert, S. D., Seinkiewicz, M., and Zhao, B.: The
738 Modern-Era Retrospective Analysis for Research and Applications, Version 2
739 (MERRA-2), *J. Clim.* 30, 5419–5454, 2017.

740 Haywood, J.M., Jones, A., Clarisse, L., Bourassa, A., Barnes, J., Telford, P., Bellouin, N.,
741 Boucher, O., Agnew, P., Clerbaux, C., Coheur, P., Degenstein, D., and Braesicke,
742 P.: Observations of the eruption of the Sarychev volcano and simulations using
743 the HadGEM2 climate model, *J. Geophys. Res.*, 115, D21212,
744 [doi:10.1029/2010JD014447](https://doi.org/10.1029/2010JD014447), 2010.

745 Illingworth, A. J., Barker, H. W., Beljaars, A., Ceccaldi, M., Chepfer, H., Clerbaux, N.,
746 Cole, J., Delanoë, J., Domenech, C., Donovan, D. P., Fukuda, S., Hidakata, M.,
747 Hogan, R. J., Huenerbein, A., Kollias, P., Kubota, T., Nakajima, T., Nakajima, T. Y.,
748 Nishizawa, T., Ohno, Y., Okamoto, H., Oki, R., Sato, K., Satoh, M., Shephard, M.
749 W., Velázquez-Blázquez, A., Wandinger, U., Wehr, T., and van Zadelhoff, G.-J.: The
750 Earth CARE Satellite: The Next Step Forward in Global Measurements of Clouds,
751 Aerosols, Precipitation, and Radiation, *B. Am. Meteorol. Soc.*, 96, 1311–1332,
752 <https://doi.org/10.1175/BAMS-D-12-00227.1>, 2015.

- 753 Junge, C.E., Chagnon, C.W., and Manson, J.E.: A World-wide Stratospheric Aerosol
754 Layer, *Science*, 133, 1478-1479, 1961.
- 755 Kablick, G. P., Allen, D. R., Fromm, M. D., and Nedoluha, G. E.: Australian PyroCb Smoke
756 Generates Synoptic-Scale Stratospheric Anticyclones, *Geophys. Res. Lett.*, 47,
757 e2020GL08810, <https://doi.org/10.1029/2020GL088101>, 2020.
- 758 Kar, J., Lee, K.-P., Vaughan, M. A., Tackett, J. L., Trepte, C. R., Winker, D. M., Lucker, P. L.,
759 and Getzewich, B. J.: CALIPSO level 3 stratospheric aerosol profile product:
760 version 1.00 algorithm description and initial assessment, *Atmos. Meas. Tech.*,
761 12, 6173–6191, <https://doi.org/10.5194/amt-12-6173-2019>, 2019.
- 762 Kloss, C., Berthet, G., Sellitto, P., Ploeger, F., Taha, G., Tidiga, M., Eremenko, M.,
763 Bossolasco, A., Jégou, F., Renard, J.-B., and Legras, B.: Stratospheric aerosol
764 layer perturbation caused by the 2019 Raikoke and Ulawun eruptions and their
765 radiative forcing, *Atmos. Chem. Phys.*, 21, 535–560, <https://doi.org/10.5194/acp-21-535-2021>, 2021.
- 767 Kovilakam, M., Thomason, L.W., Ernest, N., Rieger, L.A., Bourassa, A.E., and Millán, L.:
768 The Global Space-based Stratospheric Aerosol Climatology (version 2.0): 1979–
769 2018, *Earth Syst. Sci. Data*, 12, 2607–2634, <https://doi.org/10.5194/essd-12-2607-2020>, 2020.
- 771 Kovilakam, M., Thomason, L.W., and Knepp, T.: SAGEIII/ISS aerosol/cloud categorization
772 and its impact on GloSSAC, *Atmos. Meas. Tech.*, 16, 2709–2731,
773 <https://doi.org/10.5194/amt-16-2709-2023>, 2023.
- 774 Kremser, S., Thomason, L. W., von Hobe, M., Hermann, M., Desher, T., Timmreck, C.,
775 Toohey, M., Stenke, A., Schwarz, J. P., Weigel, R., Fueglistaler, S., Prata, F. J.,
776 Vernier, J. P., Schlager, H., Barnes, J. E., Antuña-Marrero, J. C., Fairlie, D., Palm,
777 M., Mahieu, E., Notholt, J., Rex, M., Bingen, C., Vanhellemont, F., Bourassa, A.,
778 Plane, J. M. C., Klocke, D., Carn, S. A., Clarisse, L., Trickl, T., Neely, R., James, A.
779 D., Rieger, L., Wilson, J. C., and Meland, B.: Stratospheric aerosol– Observations,
780 processes, and impact on climate, *Rev. Geophys.*, 54, 278–335,
781 <https://doi.org/10.1002/2015RG000511>, 2016.
- 782 Li, C., Krotkov, N.A., Carn, S., Zhang, Y., Spurr, R.D.J., and Joiner, J.: New-generation
783 NASA Aura Ozone Monitoring Instrument (OMI) volcanic SO₂ dataset: algorithm
784 description, initial results, and continuation with the Suomi-NPP Ozone Mapping
785 and Profiler Suite (OMPS), *Atmos. Meas. Tech.*, 10, 445–458, [www.atmos-meas-
786 tech.net/10/445/2017/](http://www.atmos-meas-tech.net/10/445/2017/), doi:10.5194/amt-10-445-2017, 2017.
- 787 Lin, P., and Fu, Q., Changes in various branches of the Brewer–Dobson circulation from
788 an ensemble of chemistry climate models, *J. Geophys. Res.*, 118, 73–84,
789 doi:10.1029/2012JD018813, 2013.
- 790 Malinina, E., Rozanov, A., Niemayer, U., Wallis, S., Arosio, C., Wrana, F., Timmreck, C.,
791 von Savigny, C., and Burrows, J.P.: Changes in stratospheric aerosol extinction

792 coefficient after the 2018 Ambae eruption as seen by OMPS-LP and MAECHAM5-
793 HAM, *Atmos. Chem. Phys.*, 21, 14871–14891, [https://doi.org/10.5194/acp-21-](https://doi.org/10.5194/acp-21-14871-2021)
794 14871-2021, 2021.

795 Martinsson, B. G., Nguyen, H. N., Brenninkmeijer, C. A. M., Zahn, A., Heintzenberg, J.,
796 Hermann, M., and Velthoven, P. F. J. v.: Characteristics and origin of lowermost
797 stratospheric aerosol at northern midlatitudes under volcanically quiescent
798 conditions based on CARIBIC observations, *J. Geophys. Res.*, 110, D12201,
799 doi:10.1029/2004JD005644, 2005.

800 Martinsson, B. G., Brenninkmeijer, C. A. M., Cam, S. A., Hermann, M., Heue, K.P., van
801 Velthoven, P. F. J., and Zahn, A.: Influence of the 2008 Kasatochi volcanic
802 eruption on sulfurous and carbonaceous aerosol constituents in the lower
803 stratosphere, *Geophys. Res. Lett.*, 36, 1–5,
804 <https://doi.org/10.1029/2009GL038735>, 2009.

805 Martinsson, B. G., Friberg, J., Sandvik, O. S., Hermann, M., van Velthoven, P. F. J., and
806 Zahn, A.: Particulate sulfur in the upper troposphere and lowermost
807 stratosphere– sources and climate forcing, *Atmos. Chem. Phys.*, 17, 10937–
808 10953, [https://doi.org/10.5194/acp-17-10937-](https://doi.org/10.5194/acp-17-10937-2017)2017, 2017.

809 Martinsson, B. G., Friberg, J., Sandvik, O. S., Hermann, M., van Velthoven, P. F. J., and
810 Zahn, A.: Formation and composition of the UTLS aerosol, *npj Climate and
811 Atmospheric Science*, 2, 1–6, <https://doi.org/10.1038/s41612-019-0097-1>, 2019.

812 Martinsson, B. G., Friberg, J., Sandvik, O. S., and Sporre, M. K.: Five-satellite-sensor
813 study of the rapid decline of wildfire smoke in the stratosphere, *Atmos. Chem.
814 Phys.*, 22, 3967–3984, [https://doi.org/10.5194/acp-22-3967-](https://doi.org/10.5194/acp-22-3967-2022)2022, 2022.

815 Martinsson, B. G., Friberg, J., and Sporre, M. K.: Stratospheric aerosol formed by intense
816 volcanism–sea interaction during the 2022 Hunga Ha’apai eruption, *Atmos.
817 Chem. Phys.*, 25, 10677–10690, [https://doi.org/10.5194/acp-25-10677-](https://doi.org/10.5194/acp-25-10677-2025)2025,
818 2025.

819 Mastin, L. G., Van Eaton, A. R., and Cronin, S. J.: Did steam boost the height and growth
820 rate of the giant Hunga eruption plume?, *B. Volcanol.*, 86, 64,
821 <https://doi.org/10.1007/s00445-024-01749-1>, 2024.

822 McCarthy, G.J., Plucinski, M.P., and Gould, J.S.: Analysis of the resourcing and
823 containment of multiple remote fires: The Great Divide Complex of fires, Victoria,
824 December 2006, *Australian Forestry*, 75, 54-63, DOI:
825 10.1080/00049158.2012.10676385, 2012.

826 Mote, P.W., Dunkerton, T.J., McIntyre, M.E., Ray, E.A., Haynes, P.H., and Russell III, J.M.:
827 Vertical velocity, vertical diffusion, and dilution by midlatitude air in the tropical
828 lower stratosphere, *J. Geophys. Res.* 103, 8651-8666, 1998.

829 Murphy, D. M., Cziczo, D. J., Hudson, P. K., and Thomson, D. S.: Carbonaceous material
830 in aerosol particles in the lower stratosphere and tropopause region, *J. Geophys.*
831 *Res.*, 112, D04203, <https://doi.org/10.1029/2006JD007297>, 2007.

832 NASA/LARC/SD/ASDC: Science CALIPSO Lidar Level 1B profile data, V4-51, NASA
833 Langley Atmospheric Data Center DAAC,
834 https://doi.org/10.5067/CALIOP/CALIPSO/CAL_LID_L1 Standard-V4-51, 2024.

835 Nicknish, P.A., Stone, K., Solomon, S., and Carn, S.A.: Quantifying the decay timescale
836 of volcanic sulfur dioxide in the stratosphere, *Atmos. Chem. Phys.*, 25, 11535–
837 11555, <https://doi.org/10.5194/acp-25-11535-2025>, 2025.

838 Ohneiser, K., Ansmann, A., Baars, H., Seifert, P., Barja, B., Jimenez, C., Radenz, M.,
839 Tiesseire, A., Floutsi, A., Haarig, M., Foth, A., Chudnovsky, A., Engelmann, R.,
840 Zamorano, F., Bühl, J., and Wandinger, U.: Smoke of extreme Australian bushfires
841 observed in the stratosphere over Punta Arenas, Chile, in January 2020: optical
842 thickness, lidar ratios, and depolarization ratios at 355 and 532nm, *Atmos.*
843 *Chem. Phys.*, 20, 8003–8015, <https://doi.org/10.5194/acp-20-8003-2020>, 2020.

844 Pardini, F., Burton, M., Arzilli, F., La Spina, G., and Polacci, M.: SO₂ emissions, plume
845 heights and magmatic processes inferred from satellite data: The 2015 Calbuco
846 eruptions, *J. Volcanol. Geotherm. Res.* 361, 12-24, 2018.

847 Peterson, D. A., Fromm, M. D., McRae, R. H. D., Campbell, J. R., Hyer, E. J., Taha, G.,
848 Camacho, C. P., Kablick, G. P., Schmidt, C. C., and DeLand, M. T.: Australia's
849 Black Summer pyrocumulonimbus super outbreak reveals potential for
850 increasingly extreme stratospheric smoke events, *Npj Clim. Atmos. Sci.*, 4, 38
851 <https://doi.org/10.1038/s41612-021-00192-9>, 2021.

852 Peterson, D. A., Berman, M. T., Fromm, M. D., Servranckx, R., Julstrom, W. J., Hyer, E. J.,
853 Campbell, J. R., McHardy, T. M., and Lambert, A.: Worldwide inventory reveals
854 the frequency and variability of pyrocumulonimbus and stratospheric smoke
855 plumes during 2013–2023, *Npj Clim. Atmos. Sci.*, 8, 325,
856 <https://doi.org/10.1038/s41612-025-01188-5>, 2025.

857 Ploeger, F., Diallo, M., Charlesworth, E., Konopka, P., Legras, B., Laube, J.C., Gross, J.-U.,
858 Günther, G., Engel, A., and Riese, M.: The stratospheric Brewer–Dobson
859 circulation inferred from age of air in the ERA5 reanalysis, *Atmos. Chem. Phys.*,
860 21, 8393–8412, <https://doi.org/10.5194/acp-21-8393-2021>, 2021.

861 Prata, A. T., Young, S. A., Siems, S. T., and Manton, M. J.: Lidar ratios of stratospheric
862 volcanic ash and sulfate aerosols retrieved from CALIOP measurements, *Atmos.*
863 *Chem. Phys.*, 17, 8599–8618, <https://doi.org/10.5194/acp-17-8599-2017>, 2017.

864 Rieger, L.A., Bourassa, A.E., and Degenstein, D.A.: Merging the OSIRIS and SAGE II
865 stratospheric aerosol records, *J. Geophys. Res. Atmos.*, 120, 8890–8904,
866 doi:10.1002/2015JD023133, 2015.

- 867 Sandvik, O. S., Friberg, J., Sporre, M. K., and Martinsson, B. G.: Methodology to obtain
 868 highly resolved SO₂ vertical profiles for representation of volcanic emissions in
 869 climate models, *Atmos. Meas. Tech.*, 14, 7153–7165,
 870 <https://doi.org/10.5194/amt-14-7153-2021>, 2021.
- 871 Sato, M., Hansen, J.E., McCormick, M.P., and Pollack J.B.: Stratospheric aerosol optical
 872 depths, 1850-1990, *J. Geophys. Res.* 98, 22987-22994, 1993.
- 873 Schmidt, A., Mills, M. J., Ghan, S., Gregory, J. M., Allan, R. P., Andrews, T., Bardeen, C. G.,
 874 Conley, A., Forster, P. M., Gettelman, A., Portmann, R. W., Solomon, S., and Toon,
 875 O. B.: Volcanic radiative forcing from 1979 to 2015, *J. Geophys. Res.-Atmos.*, 123,
 876 12491–12508, <https://doi.org/10.1029/2018JD028776>, 2018.
- 877 Seabrook, S., Mackay, K., Watson, S. J., Clare, M. A., Hunt, J. E., Yeo, I. A., Lane, E. M.,
 878 Clark, M. R., Wysoczanski, R., Rowden, A.A., Kula, T., Hoffmann, L.J., Armstrong,
 879 E., and Williams, M. J. M.: Volcaniclastic density currents explain widespread
 880 and diverse seafloor impacts of the 2022 Hunga Volcano eruption, *Nat.*
 881 *Commun.*, 14, 7881, <https://doi.org/10.1038/s41467-023-43607-2>, 2023.
- 882 Sheng, J.-X., Weisenstein, D.K., Luo, B.-P., Rozanov, E., Stenke, A., Anet, J., Bingemer, H.,
 883 and Peter, T.: Global atmospheric sulfur budget under volcanically quiescent
 884 conditions: Aerosol-chemistry-climate model predictions and validation, *J.*
 885 *Geophys. Res. Atmos.*, 120, 256–276, doi:10.1002/2014JD021985, 2015.
- 886 Solomon, S., Daniel, J. S., Neely, R. R., Vernier, J.-P., Dutton, E. G., and Thomason, L. W.:
 887 The persistently variable “background” stratospheric aerosol layer and global
 888 climate change, *Science*, 333, 866–870, 2011.
- 889 Solomon S., Dube K., Stone K., Yu P., Kinnison D., Toon O.B., Strahan S.E., Rosenlov
 890 K.H., Portmann R., Davis S., Randel W., Bernath P., Boone C., Bardeen C.G.,
 891 Bourassa A., Zawada D., and Degenstein D.: On the stratospheric chemistry of
 892 midlatitude wildfire smoke, *Proc. Natl. Acad. Sci. U.S.A.* 119, E2117325119,
 893 <https://doi.org/10.1073/pnas.2117325119>, (2022).
- 894 Surano, Jousset, P., Pallister, J., Boichu, M., Bongiorno, M.F., Budisantoso, A., Costa, F.,
 895 Andreastuti, S., Prata, F., Schneider, D., Clarisse, L., Humaida, H., Sumarti, S.,
 896 Bignami, C., Griswold, J., Carn, S., Oppenheimer C., and Lavigne F.: The 2010
 897 explosive eruption of Java's Merapi volcano—A ‘100-year’ event, *J. Volcanol.*
 898 *Geotherm. Res.* 241-242, 121-135, 2012.
- 899 Taylor, I. A., Grainger, R. G., Prata, A. T., Proud, S. R., Mather, T. A., and Pyle, D. M.: A
 900 satellite chronology of plumes from the April 2021 eruption of La Soufrière, St
 901 Vincent, *Atmos. Chem. Phys.*, 23, 15209–15234, [https://doi.org/10.5194/acp-23-](https://doi.org/10.5194/acp-23-15209-2023)
 902 [15209-2023](https://doi.org/10.5194/acp-23-15209-2023), 2023.
- 903 Thomas, H.E., Watson, I.M., Carn, S.A., Prata, A.J., and Realmuta, V.J.: A comparison of
 904 AIRS, MODIS and OMI sulphur dioxide retrievals in volcanic clouds, *Geomatics,*
 905 *Natural Hazards and Risk*, 2, 217-232, 2011.

906 Thomason, L.W., Ernest, N., Millán, L., Rieger, L., Bourassa, A., Vernier, J.-P., Manney, G.,
907 Luo, B., Arfeuille, F., and Peter, T.: A global space-based stratospheric aerosol
908 climatology: 1979-2016, *Earth Syst. Sci. Data*, 10, 469–492,
909 <https://doi.org/10.5194/essd-10-469-2018>, 2018.

910 Vernier, J.-P., Pommereau, J.P., Garnier, A., Pelon, J., Larsen, N., Nielsen, J.,
911 Christiansen, T., Cairo, F., Thomason, L.W., Leblanc, T., and McDermid, I.S.:
912 Tropical stratospheric aerosol layer from CALIPSO lidar observations, *J.*
913 *Geophys. Res.*, 114, D00H10, doi:10.1029/2009JD011946, 2009.

914 Vernier, J.-P., Farlie, T.D., Murray, J.J., Tupper, A., Trepte, C., Winker, D., Pelon, J., Garnier,
915 A., Jumelet, J., Pavolonis, M., Omar, A.H., and Powell, K.A.: An Advanced System
916 to Monitor the 3D Structure of Diffuse Volcanic Ash Clouds *J. Appl. Meteorol.*
917 *Clim.* 10, 2125-2138, 2013.

918 Vernier, J.-P., Farlie, T.D., Natarajan, M., Wiengold, F.G., Bian, J., Martinsson, B.G.,
919 Crumeyrolle, S., Thomason, L.W., and Bedka, K.M.: Increase in upper
920 tropospheric and lower stratospheric aerosol levels and its potential connection
921 with Asian pollution, *J. Geophys. Res.*, 120, doi:10.1002/2014JD022372, 2015.

922 Weisenstein, D.K., Yue, G.K., Ko, M.K.W., Sze, N.-D., Rodriguez, J.M., and Scott, C.J.: A
923 two-dimensional model of sulfur species and aerosol, *J. Geophys. Res.* 102,
924 13019-13035, 1997.

925 Winker, D. M., Hunt, W. H., and McGill, M. J.: Initial performance assessment of CALIOP,
926 *Geophys. Res. Lett.*, 34, 1–5, <https://doi.org/10.1029/2007GL030135>, 2007.

927 Winker, D. M., Pelon, J., Coakley, J. A., Ackerman, S. A., Charlson, R. J., Colarco, P. R.,
928 Flamant, P., Fu, Q., Hoff, R. M., Kittaka, C., Kubar, T. L., Le Treut, H., McCormick,
929 M. P., Mégie, G., Poole, L., Powell, K., Trepte, K., Vaughan, M. A., and Wielicki, B.
930 A.: The CALIPSO mission—A global 3D view of aerosols and clouds, *B. Am.*
931 *Meteorol. Soc.*, 91, 1211–1229, <https://doi.org/10.1175/2010BAMS3009.1>, 2010.

932

933 **Tables**934 **Table 1.** Major volcanic eruptions and wildfires affecting the stratospheric aerosol in the
935 CALIOP era.

	Date	Volcano/wildfire	Lat ^a	Lon ^b	SO ₂ (Tg)	References
<i>Volcanic eruptions</i>						
1	2006-05-20	Soufriere Hills (Su)	17°	-62.2°	0.2	Carn and Prata (2010)
2	2006-10-07	Rabaul (Rb)	-4°	152°	0.23	Carn et al. (2009)
3	2008-08-07	Kasatochi (Ka)	52°	-176°	1.7	Thomas et al. (2011)
4	2009-06-12	Sarychev (Sa)	48°	153°	1.2	Haywood et al. (2010)
5	2010-10-05	Merapi (Me)	-7°	110°	0.44	Surono et al. (2012)
6	2011-06-05	Puyehue-Cordón Caulle (Pu)	-40°	-72°	0.25	Clarisse et al. (2012)
7	2011-06-12	Nabro (Na)	13°	42°	1.5	Clarisse et al. (2012)
8	2014-02-13	Kelut (Ke)	-8°	112°	0.18	Li et al. (2017)
9	2015-04-23	Calbuco (Ca)	-41°	-73°	0.3	Pardini et al. (2018)
10	2018-07-27	Ambae (Am)	-15°	168°	0.36	Malinina et al. (2021)
11	2019-06-22	Raikoke (Ra)	48°	153°	1.5	Kloss et al. (2021)
12	2019-06-26	Ulawun (Ul)	-5°	151°	0.14	Kloss et al. (2021)
13	2019-08-03	Ulawun (Ul)	-5°	151°	0.3	Kloss et al. (2021)
14	2021-04-10	Soufriere (So)	13°	-61°	0.31	Taylor et al. (2023)
15	2022-01-15	Hunga Ha'apai (Hu)	-21°	175°	0.45	Carn et al. (2022)
<i>Wildfires</i>						
16	2006-12-19	Australia (A1)	-37°	147°	-	McCarthy et al. (2012)
17	2009-02-07	Australia (A2)	-38°	146°	-	Cruz et al. (2012)
18	2017-08-12	Canada/USA (CU)	53°	-123°	-	Fromm et al. (2021)
19	2019-12-29	Australia (A3)	-37°	149°	-	Peterson et al. (2021)
20	2020-01-04	Australia (A4)	-37°	149°	-	Peterson et al. (2021)

936

937

938

939 **Table 2.** Average backscattering of background aerosol and AOD of aerosol events in
940 2006 - 2023 and the distribution over nine stratospheric layers.

Backscattering background ^a				
	<i>Global</i>	SH	Tropics	NH
<i>Total</i>		40%	21%	39%
dBD	39%	13%	14%	12%
sBD	37%	15%	7.3%	15%
LMS	24%	12%	0.2%	11%

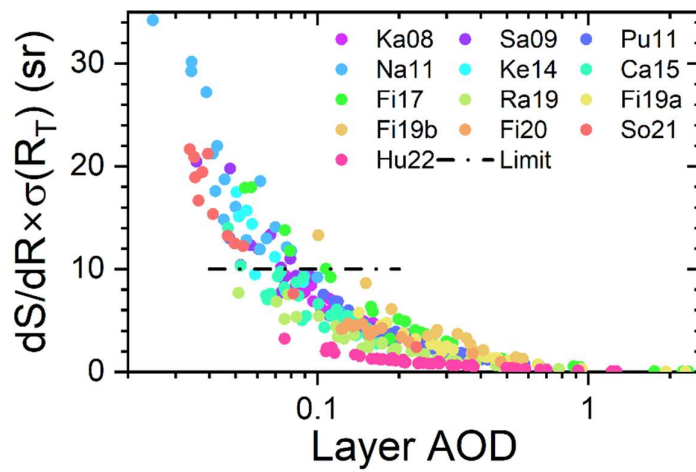
AOD aerosol events ^b				
	<i>Global</i>	SH	Tropics	NH
<i>Total</i>		33%	31%	35%
dBD	31%	9.0%	18%	4.0%
sBD	43%	15%	13%	15%
LMS	26%	9.0%	0.4%	17%

941 ^aAverage backscattering of background = 0.00011 sr⁻¹

942 ^bAverage AOD from aerosol events (2006 – 2023) = 0.0031

943

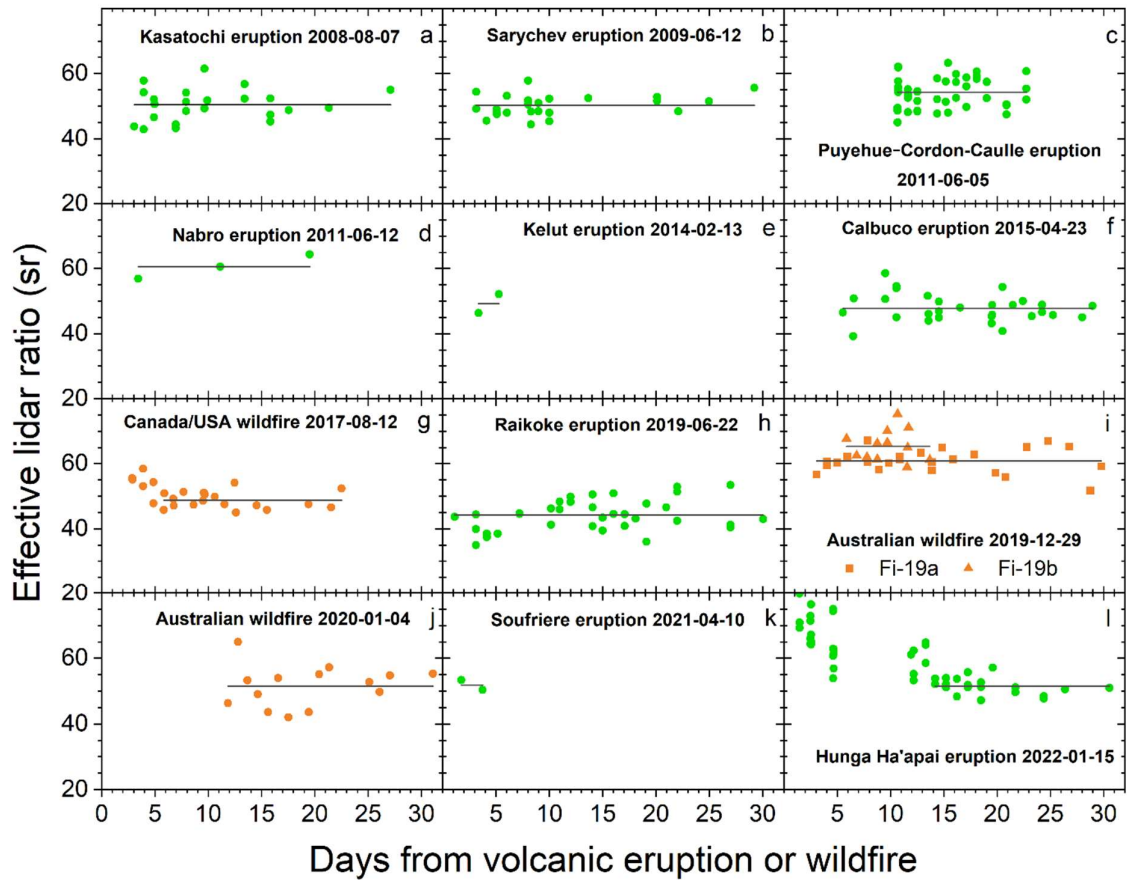
944 **Figure captions**



945

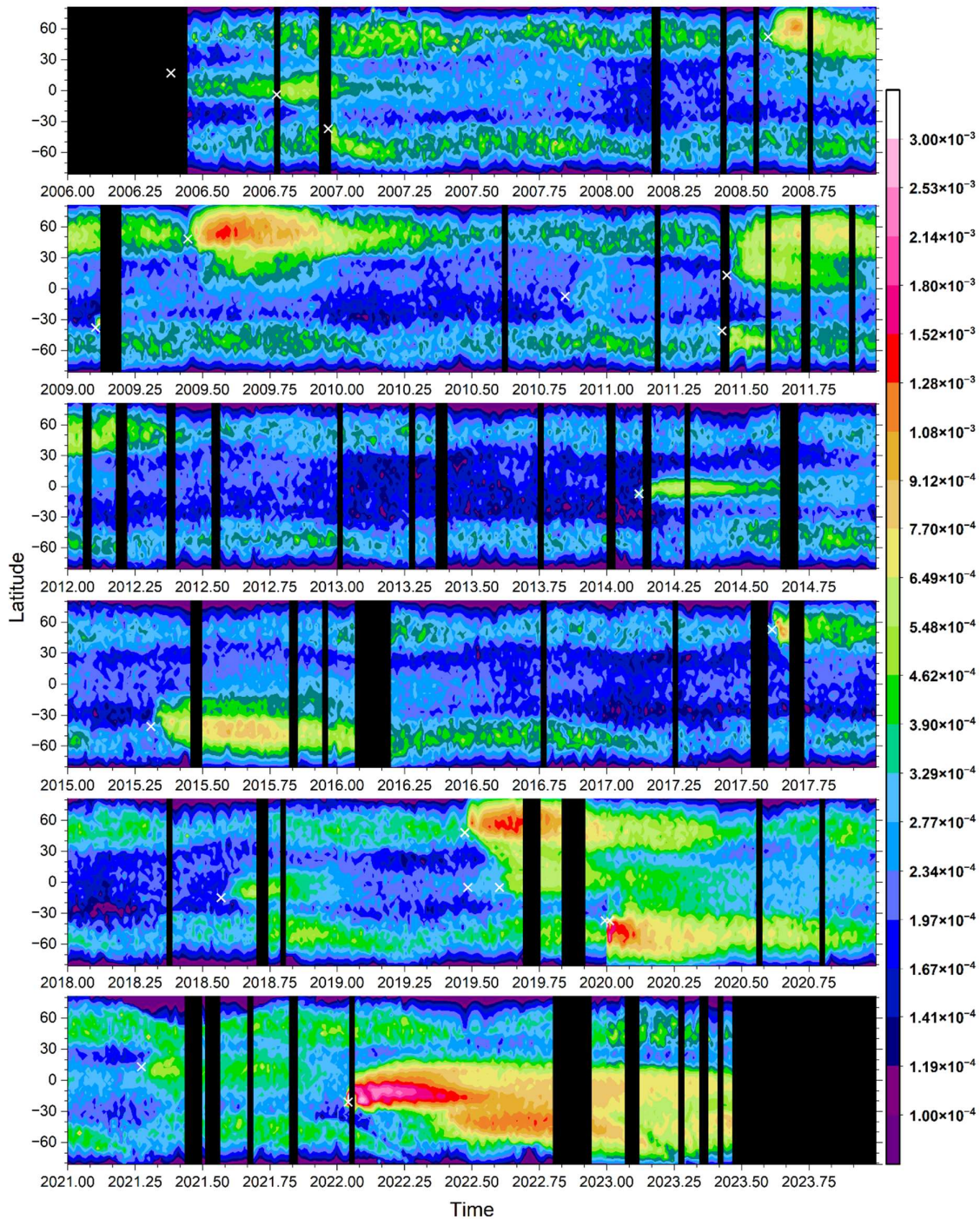
946 **Figure 1.** Relation between the layer AOD and the measure on the uncertainty of the
947 lidar ratio estimation. dS/dR is the sensitivity of the lidar ratio (S) to small shifts of the
948 target scattering ratio (R) and $\sigma(R_T)$ is the standard deviation of the target R of each
949 eruption or wildfire obtained horizontally beside each aerosol layer investigated. Layers
950 with uncertainty exceeding 10 sr (“limit”) are discarded in the following analysis.

951



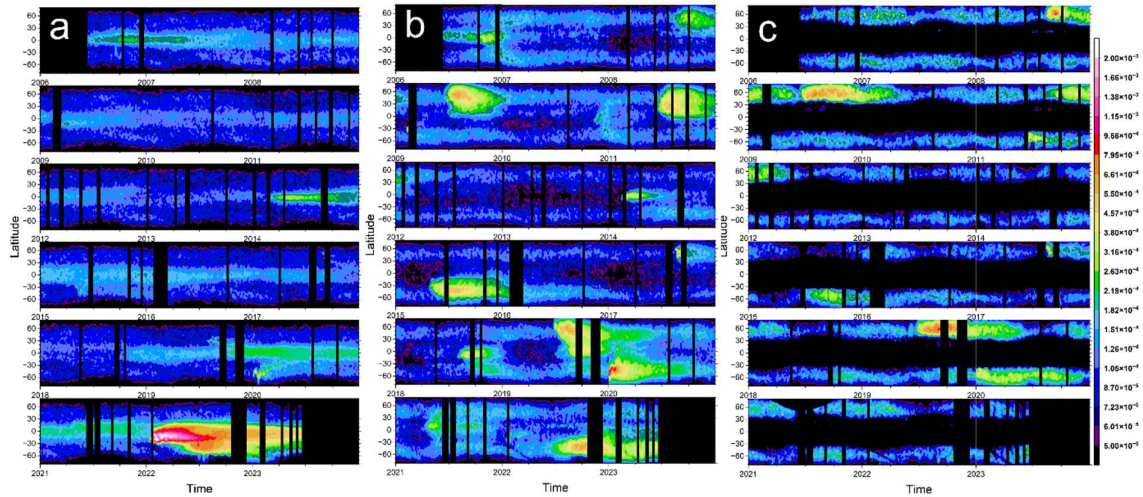
952

953 **Figure 2.** Effective particle lidar ratios the first 30 days after a volcanic eruption or
 954 wildfire with a line displaying the average of each event. All measurements concurring
 955 with the condition $dS/dR \times \sigma(R) < 10$ are displayed for volcanic eruptions and wildfires in
 956 a) to l). The averages include all data points except for the Canada/USA wildfire (g) and
 957 the Hunga Ha'apai eruption (l) where the initial decline in the lidar ratio is not part of the
 958 average represented by horizontal lines.



959

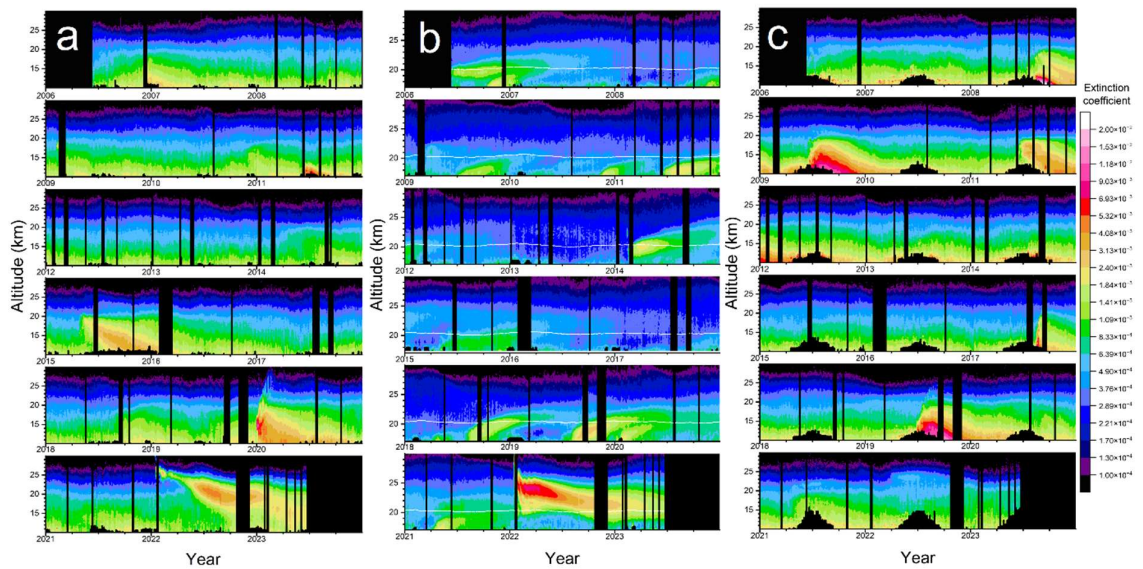
960 **Figure 3.** AOD integrated from the tropopause to 35 km altitude averaged over 4 days
 961 and 3 degrees in latitude. The lidar ratio is set to 50 sr. Color scale: The data is latitude
 962 weighted in the way that the global AOD contribution per degree of latitude is shown, i.e.
 963 the sum over latitude is the total AOD at any given time. The data has been extrapolated
 964 at high latitudes as described in section 2.1, Figure S7 shows the data without
 965 extrapolation. White crosses indicate time and latitude of aerosol events mentioned in
 966 Table 1.



967

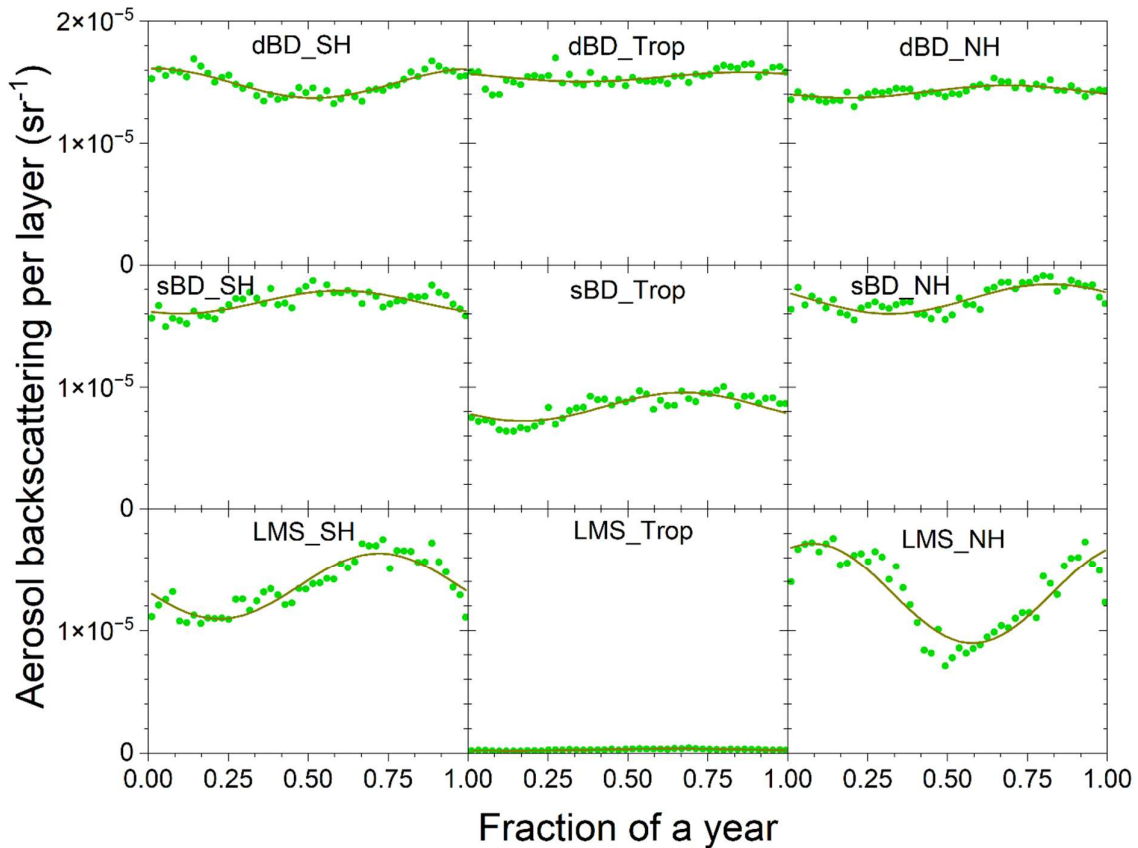
968 **Figure 4.** AOD integrated in three layers: a) dBD, b) sBD and c) LMS. The color scale is
 969 latitude weighted as explained in the caption of Figure 3. Full size images are displayed
 970 in the Supplementary material, Figures S1 – S3.

971



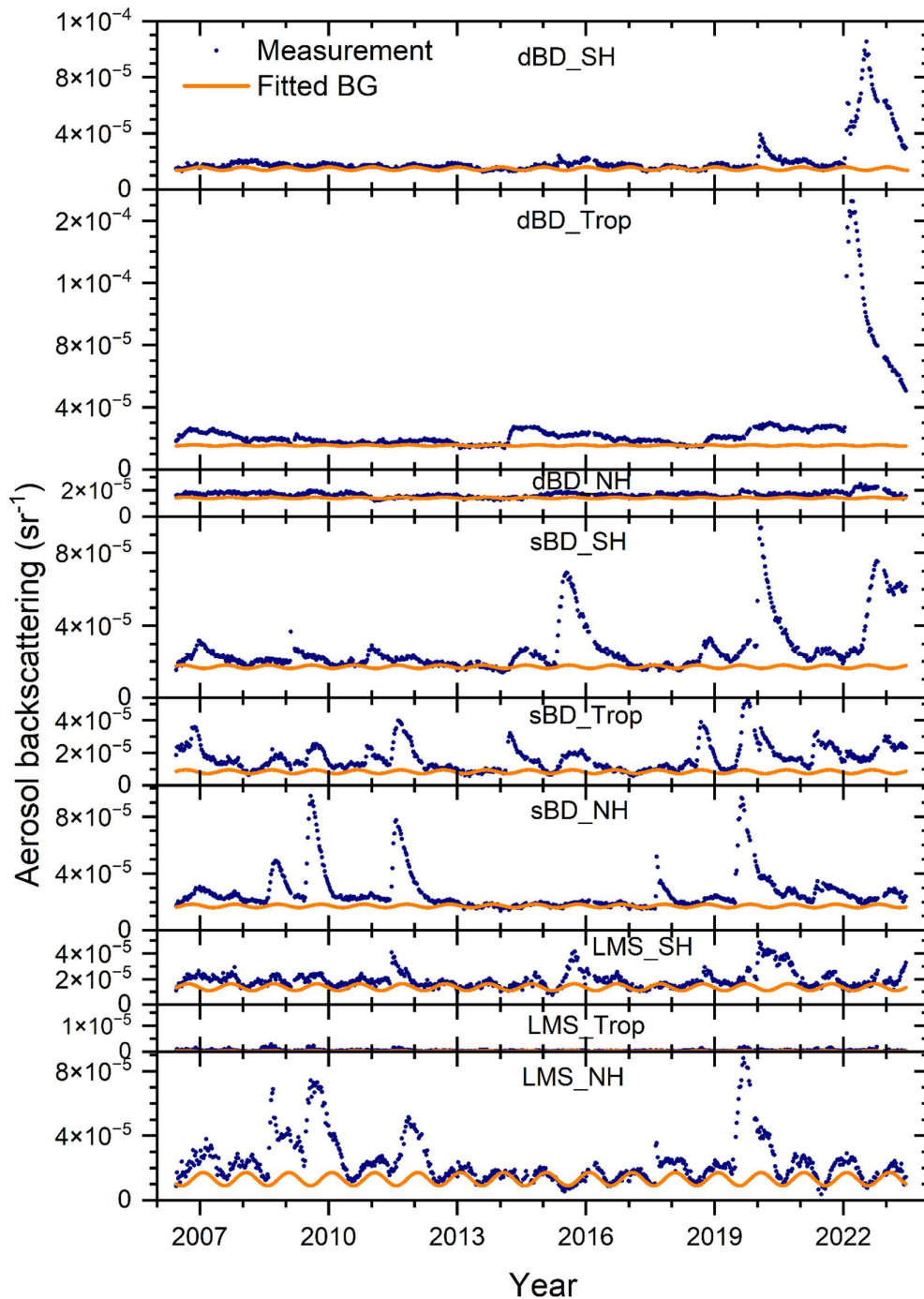
972

973 **Figure 5.** Extinction coefficients (km^{-1}) averaged in three latitude bands: a) southern
 974 extratropics (-80 to -20°), b) tropics (-20 to 20°) and c) northern extratropics (20 to 80°).
 975 Full size images are displayed in the Supplementary material, Figures S4 – S6.



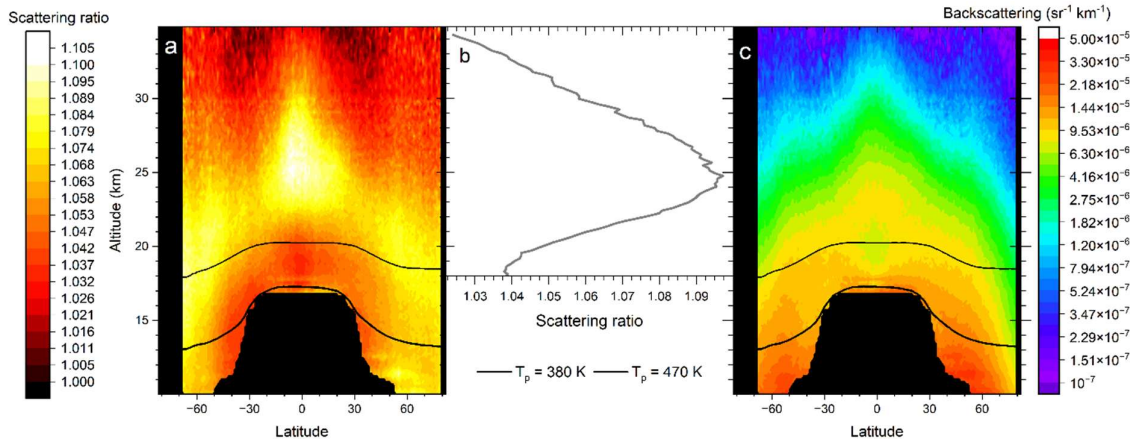
976

977 **Figure 6.** Average backscattering, which when multiplied with the lidar ratio becomes
 978 the AOD of the layer, of the background aerosol extracted based on the three lowest
 979 average values of each 8-day period over the year in the CALIOP era (2006 – 2023). The
 980 extracted data were fitted to a constant and a sinusoidal function. (Exceptions: the two
 981 lowest 8-day averages were used for “dBD_Trop” and “sBD_Trop” due to infrequent
 982 background values.) The extraction was undertaken in nine regions spanned by
 983 latitudes: -80 to -20° (SH), -20 to 20° (Tropics), 20 to 80° (NH) and altitude ranges: the
 984 tropopause to 380 K isentrope (LMS), 380 to 470 K isentrope (sBD), 470 K to 35 km
 985 altitude (dBD). The data were latitude weighted in the way that the sum of the nine
 986 layers is the global aerosol backscattering.



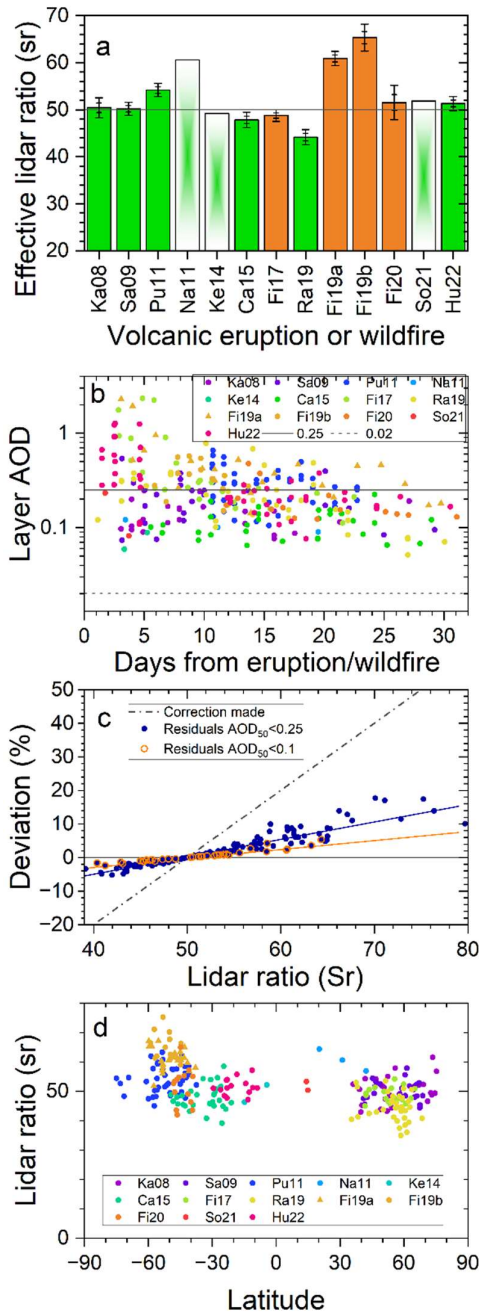
987

988 **Figure 7.** Stratospheric aerosol average backscattering, which when multiplied with the
 989 lidar ratio becomes the AOD, and fitted background in nine latitude and altitude regions:
 990 the deep BD branch (470 K isentrope to 35 km altitude), the shallow BD branch
 991 (between isentropes 380 and 470 K) and the LMS (from the tropopause to the 380 K
 992 isentrope) and three latitude regions the southern hemisphere extratropics (-80 to -20°),
 993 the tropics (-20 to 20°) and the northern hemisphere extratropics (20 to 80°) to find time-
 994 sections not or weakly affected by stratospheric aerosol events (see Fig. 4 and text for
 995 details).



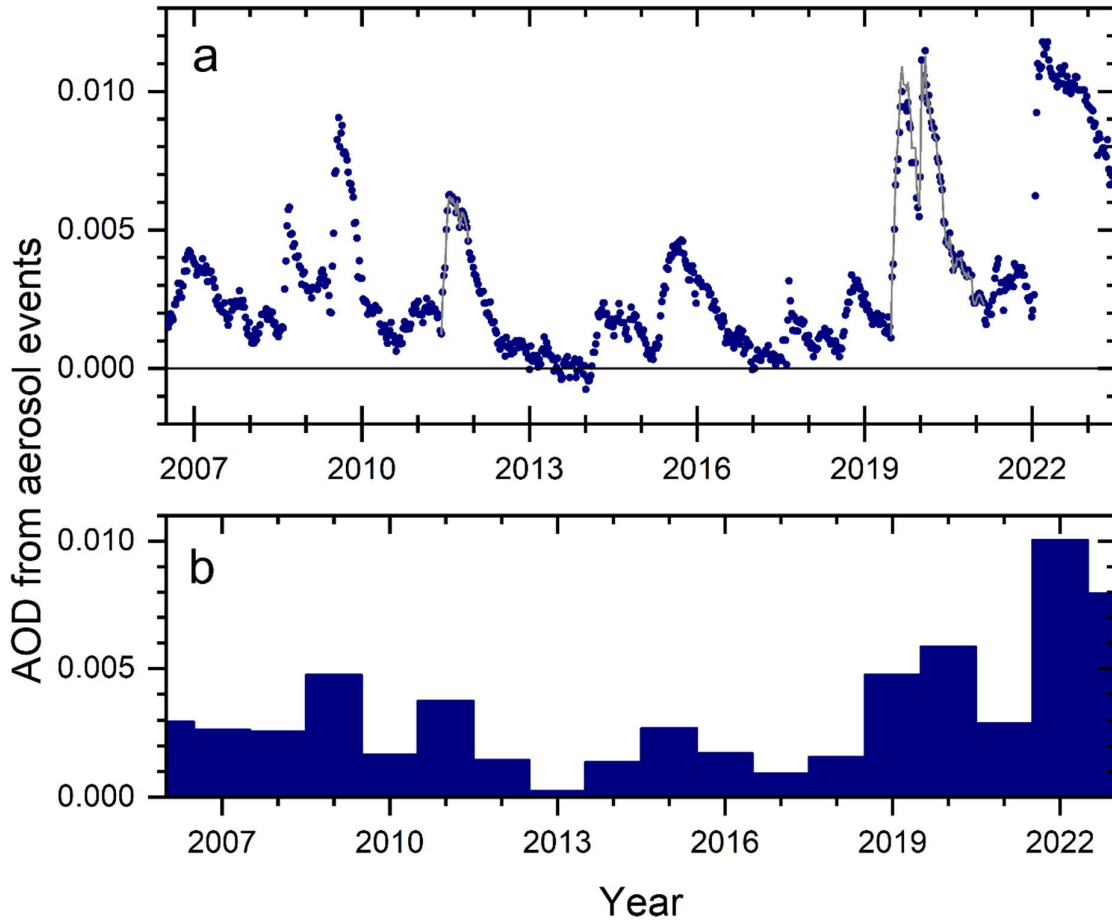
996

997 **Figure 8.** The stratospheric aerosol averaged over year 2013, which was close to
 998 background conditions. a) The scattering ratio, i.e., the ratio between the total to the
 999 modeled backscattering of air molecules. This intensive parameter is not latitude
 1000 weighted. b) Average scattering ratio in the central tropics (latitudes -10 to 10°)
 1001 dependence on altitude. c) Average aerosol backscattering, this extensive quantity is
 1002 latitude weighted. Black lines in a) and c) are the yearly average positions of the
 1003 potential temperatures (T_p) 380 and 470 K.



1004

1005 **Figure 9.** a) Average lidar ratios according to Fig. 2 with standard errors and 95% ranges
 1006 of volcanic eruptions and wildfires. Too few observations for error estimations were
 1007 obtained for the eruptions of Nabro (Na11), Kelut (Ke14) and Soufriere (So21). b) AODs
 1008 of aerosol layers with $dS/dR \times \sigma(R) < 10$ sr Vs. time from the eruption or wildfire. The full
 1009 line illustrates approximate maximum layer AOD after 1 month, and the broken line
 1010 indicates the approximate maximum layer AOD observable by limb-viewing techniques
 1011 (note: logarithmic y-scale). c) Correction of AOD obtained by setting the lidar ratio to 50
 1012 sr (AOD_{50}), based on a linear dependence of the AOD on the lidar ratio. The residual
 1013 deviation after the correction of two categories is also shown: aerosol layers with AOD_{50}
 1014 < 0.1 and < 0.25 . d) Estimated lidar ratios in Figure 2 Vs. latitude.



1015

1016 **Figure 10.** Background-subtracted AOD of the stratosphere from the tropopause to 35
 1017 km altitude and averaged from -80 to 80° in latitude. a) AOD from main stratospheric
 1018 aerosol events caused by volcanic eruptions and wildfires. AOD₅₀ is shown (full grey
 1019 line) where correction due to lidar ratio deviating from 50 sr is undertaken (Pu11, Ra19
 1020 and Fi19&20). b) Yearly averages of data in a). Note that the horizontal tick marks
 1021 indicate start of a year in a) and the middle of a year in b). Also note that the averages of
 1022 years 2006 and 2023 span only half years due to the mid-year start (2006) and finish
 1023 (2023) of the CALIOP measurements.